Article

Cell Reports

Breast Cancer-Derived Lung Metastases Show Increased Pyruvate Carboxylase-Dependent Anaplerosis

Graphical Abstract

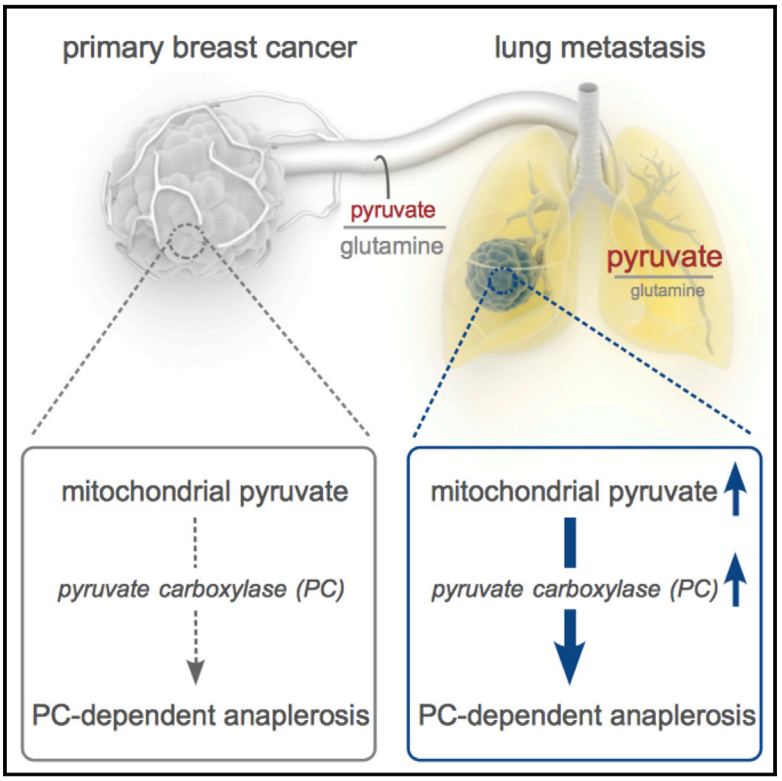

Highlights

- Lung metastases have higher PC-dependent anaplerosis than primary breast cancers
- PC-dependent anaplerosis is a function of the in vivo microenvironment
- Pyruvate to glutamine availability is increased in the in vivo lung microenvironment
- Compartment-specific pyruvate distributions can be inferred from ^{13}C labeling patterns

Authors

Stefan Christen, Doriane Lorendeau, Roberta Schmieder, ..., Thomas Georg Philipp Grünewald, Katrien De Bock, Sarah-Maria Fendt

Correspondence

sarah-maria.fendt@vib-kuleuven.be

In Brief

Christen et al. find that primary breast cancers and their resulting lung metastases use different modes of TCA cycle anaplerosis. Lung metastases increase PC-dependent anaplerosis in response to the in vivo lung microenvironment. Mechanistically, this response is mediated by alterations in PC expression and mitochondrial pyruvate concentrations.

Christen et al., 2016, Cell Reports *17*, 837–848
October 11, 2016
http://dx.doi.org/10.1016/j.celrep.2016.09.042

CellPress

Cell Reports
Article

Breast Cancer-Derived Lung Metastases Show Increased Pyruvate Carboxylase-Dependent Anaplerosis

Stefan Christen,[1,2] Doriane Lorendeau,[1,2] Roberta Schmieder,[1,2] Dorien Broekaert,[1,2] Kristine Metzger,[1,2] Koen Veys,[3] Ilaria Elia,[1,2] Joerg Martin Buescher,[1,2] Martin Franz Orth,[4] Shawn Michael Davidson,[5] Thomas Georg Philipp Grünewald,[4] Katrien De Bock,[6] and Sarah-Maria Fendt[1,2,7,*]

[1]Laboratory of Cellular Metabolism and Metabolic Regulation, Vesalius Research Center, VIB, Herestraat 49, 3000 Leuven, Belgium
[2]Laboratory of Cellular Metabolism and Metabolic Regulation, Department of Oncology, KU Leuven and Leuven Cancer Institute (LKI), Herestraat 49, 3000 Leuven, Belgium
[3]Laboratory of Angiogenesis and Vascular Metabolism, Department of Oncology (KU Leuven) and Vesalius Research Center (VIB), Herestraat 49, 3000 Leuven, Belgium
[4]Max-Eder Research Group for Pediatric Sarcoma Biology, Institute of Pathology, LMU Munich, Thalkirchner Strasse 36, 80337 Munich, Germany
[5]David H. Koch Institute for Integrative Cancer Research, Massachusetts Institute of Technology, 500 Main Street, Cambridge, MA 02139, USA
[6]Laboratory of Exercise and Health, Department of Health Sciences and Technology, ETH Zurich, Schorenstrasse 16, 8603 Schwerzenbach, Switzerland
[7]Lead Contact
*Correspondence: sarah-maria.fendt@vib-kuleuven.be
http://dx.doi.org/10.1016/j.celrep.2016.09.042

SUMMARY

Cellular proliferation depends on refilling the tricarboxylic acid (TCA) cycle to support biomass production (anaplerosis). The two major anaplerotic pathways in cells are pyruvate conversion to oxaloacetate via pyruvate carboxylase (PC) and glutamine conversion to α-ketoglutarate. Cancers often show an organ-specific reliance on either pathway. However, it remains unknown whether they adapt their mode of anaplerosis when metastasizing to a distant organ. We measured PC-dependent anaplerosis in breast-cancer-derived lung metastases compared to their primary cancers using in vivo ^{13}C tracer analysis. We discovered that lung metastases have higher PC-dependent anaplerosis compared to primary breast cancers. Based on in vitro analysis and a mathematical model for the determination of compartment-specific metabolite concentrations, we found that mitochondrial pyruvate concentrations can promote PC-dependent anaplerosis via enzyme kinetics. In conclusion, we show that breast cancer cells proliferating as lung metastases activate PC-dependent anaplerosis in response to the lung microenvironment.

INTRODUCTION

Most proliferating cells, such as cancer cells, exploit the tricarboxylic acid (TCA) cycle for biomass precursor production (Pavlova and Thompson, 2016), a process that is critically dependent on sufficient anaplerosis. One important route to refill the TCA cycle occurs via the enzyme pyruvate carboxylase (PC), which converts pyruvate to oxaloacetate. Glycolysis-fueling nutrients such as glucose and pyruvate are in vitro and in vivo the major carbon sources providing PC with its substrate pyruvate (Davidson et al., 2016; Hensley et al., 2016; Sellers et al., 2015). The alternative route to PC-dependent anaplerosis is glutamine anaplerosis, and a reciprocal relationship between both modes of TCA cycle anaplerosis has been established (Cheng et al., 2011).

PC is transcriptionally and metabolically regulated. Several regulators such as peroxisome proliferator-activated receptor-γ, hepatocyte nuclear factor 3β, forkhead/winged helix transcription factor box2, or upstream stimulatory factors 1/2 are known to alter PC expression (Boonsaen et al., 2007). Yet, additional mechanisms exist by which PC activity is regulated on a metabolic level. These mechanisms include the inhibitory effects of glutamate and α-ketoglutarate on PC activity, but also many mechanisms that are directly or indirectly connected to pyruvate availability (Zeczycki et al., 2010). PC is a mitochondrial enzyme, and fueling of PC with glycolysis-derived pyruvate depends on the activity of the mitochondrial pyruvate carrier (MPC) (Vanderperre et al., 2015). Once pyruvate is in the mitochondria, it is available as substrate for PC and thus can promote PC activity via enzyme kinetics (Taylor et al., 1969). Moreover, pyruvate has been shown to decrease the K_m of PC for bicarbonate (McClure et al., 1971). Yet, pyruvate is not only fueling PC, but also pyruvate dehydrogenase (PDH). This conversion results in acetyl-CoA production and thus increased substrate availability for an oxidative TCA cycle, which contributes to ATP production. Both a high ATP/ADP ratio and acetyl-CoA have been shown to promote PC activity (Jitrapakdee et al., 2008; Adina-Zada et al., 2012; von Glutz and Walter,

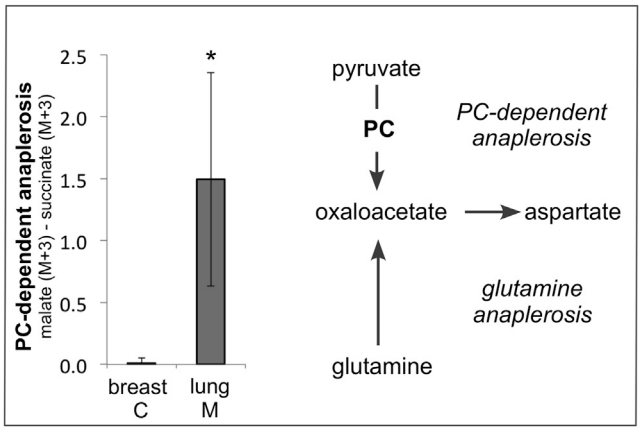

Figure 1. Lung Metastases Show Increased PC-Dependent Anaplerosis

Relative PC-dependent anaplerosis in primary breast cancers (C) and lung metastases (M) from 4T1 mice after 6 hr of infusion with $^{13}C_6$-glucose (n = 4). Mass distribution vectors are provided in Table S1. Error bars depict SD. *$p \leq 0.05$ based on a two-tailed paired t test.

1976; Walter and Stucki, 1970). Thus, transcriptional and metabolic regulation can impact PC activity and therefore pyruvate-dependent anaplerosis.

In cancers, differential in vivo preference for PC-dependent anaplerosis versus glutamine anaplerosis has been observed and linked to altered PC expression (Davidson et al., 2016; Sellers et al., 2015). The best-studied examples are breast and lung cancers. In vivo, many breast cancers show low PC-dependent anaplerosis (Deberardinis et al., 2008; Elia et al., 2016), while the majority of lung cancers show high PC-dependent anaplerosis (Fan et al., 2009; Hensley et al., 2016; Sellers et al., 2015). In addition, it has been observed that a major change in the microenvironment, such as in vivo versus in vitro cultivation, shifts *RAS*-driven lung cancer cells from PC-dependent anaplerosis to glutamine anaplerosis (Davidson et al., 2016). Consequently, only in vitro-cultured *RAS*-driven lung cancer cells are sensitive to glutamine anaplerosis inhibitors (Davidson et al., 2016). These findings highlight the importance of understanding the interaction between microenvironment and cancer metabolism to select treatments that are effective in vivo.

An in vivo process inherently linked to changes in the microenvironment is cancer progression toward metastases formation, which causes most cancer-related deaths. During metastases formation, cancer cells originating from one specific tissue and microenvironment migrate to a distant organ and resume proliferation within this new microenvironment. However, whether a change between two in vivo microenvironments is sufficient to alter PC-dependent anaplerosis in cells of the same origin, and by which mechanism this occurs, remains unexplored.

We addressed these questions by measuring PC-dependent anaplerosis in primary breast cancers and the resulting lung metastases of an orthotopic breast cancer mouse model. We found that lung metastases have increased PC-dependent anaplerosis compared to the corresponding primary breast cancers, which shows that changes in the in vivo microenvironment can enforce a change in the anaplerosis mode of cells that share the same cellular origin. Applying a mathematical model that resolves compartment-specific pyruvate concentrations, we further provide evidence that increased mitochondrial pyruvate concentrations can promote PC-dependent anaplerosis via enzyme kinetics. In conclusion, we show that breast cancer cells proliferating as lung metastases increase PC-dependent anaplerosis as a result of an altered in vivo microenvironment.

RESULTS

Lung Metastases, but Not the Primary Breast Cancers, Use PC-Dependent Anaplerosis

It has been recently shown that switching lung cancer cells from an in vitro to an in vivo microenvironment promotes PC-dependent anaplerosis (Davidson et al., 2016). Based on this observation, we asked whether cancer cells of the same cellular origin rewire their anaplerosis mode when proliferating within two different in vivo microenvironments. Such a situation is highly relevant during cancer progression when cancer cells infiltrate distant organs and give rise to metastases.

We decided to test whether breast cancers and their resulting lung metastases show a different degree of PC-dependent anaplerosis using in vivo ^{13}C tracer analysis (Davidson et al., 2016; Quaegebeur et al., 2016). For this purpose, we exploited the highly metastatic 4T1 breast cancer mouse model, which has a 100% penetrance for lung metastases within a time frame of days. Thus, if PC-dependent anaplerosis is a function of changes in the in vivo microenvironment, we expect that primary breast cancers and the resulting lung metastases show different degrees of PC-dependent anaplerosis. We infused mice bearing primary breast cancers and lung metastases with $^{13}C_6$-glucose, and we subsequently measured the ^{13}C-labeling patterns of pyruvate, succinate, and malate in the primary cancer and metastases tissue (Table S1). To estimate the relative changes in PC-dependent anaplerosis, we compared the malate M+3 and succinate M+3 from $^{13}C_6$-glucose (Buescher et al., 2015). Malate M+3 from $^{13}C_6$-glucose is generated by PC flux, but can also arise from an oxidative TCA cycle flux. Succinate M+3 from $^{13}C_6$-glucose can arise from an oxidative TCA cycle flux, but not from PC flux (given that reverse succinate dehydrogenase flux is marginal or not present). Thus, under the prerequisite that pyruvate enrichment from $^{13}C_6$-glucose is similar, comparing malate M+3 and succinate M+3 allows to conclude on relative changes of PC-dependent anaplerosis between primary breast cancers and lung metastases. We discovered that lung metastases had significantly higher PC-dependent anaplerosis compared to primary breast cancers (Figure 1). This is a striking result, because it has been shown that breast cancer cells isolated from lung metastases of the 4T1 mouse model have a similar low PC-dependent anaplerosis as the parental 4T1 breast cancer cell line when cultured in the same in vitro microenvironment (Dupuy et al., 2015). Thus, we concluded that breast cancer cells can alter their magnitude of PC-dependent anaplerosis based on a change in the in vivo microenvironment.

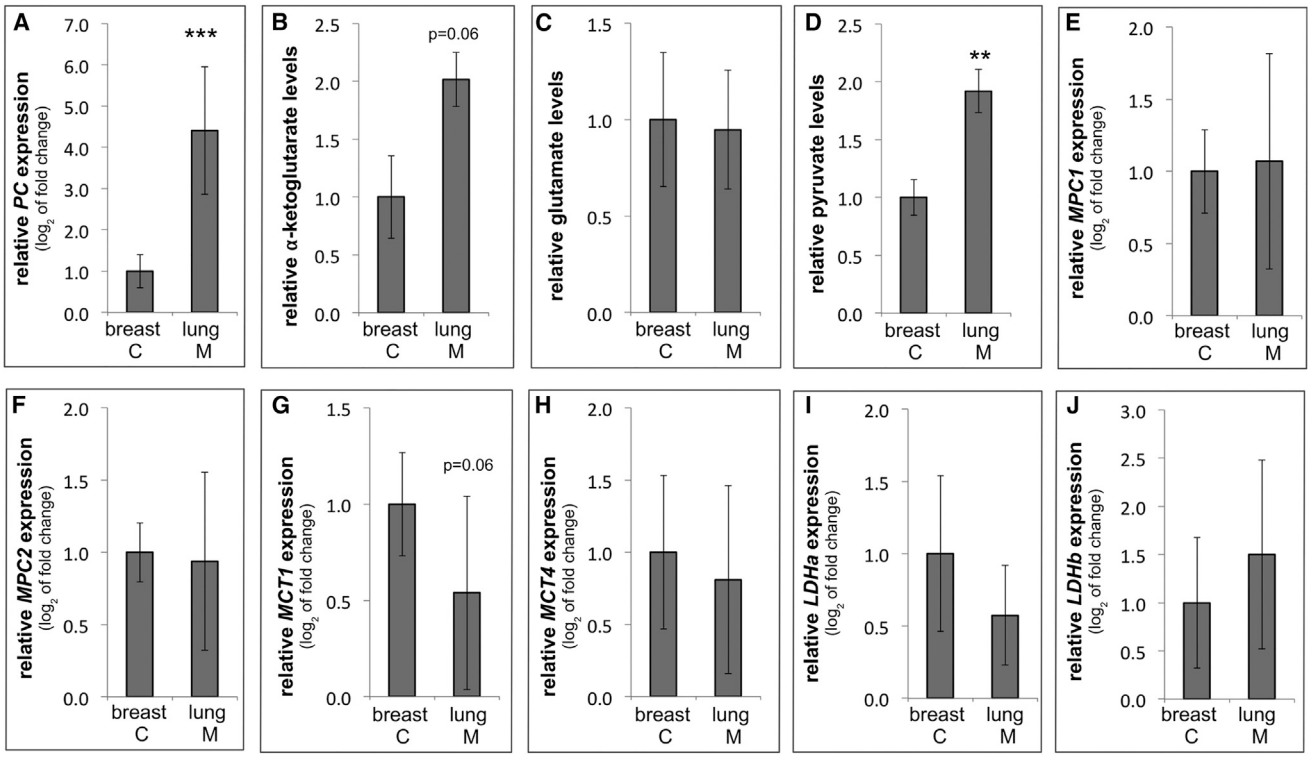

Figure 2. Pyruvate Levels and PC Expression Are Increased in Lung Metastases

(A and E–J) Relative expression of *PC*, *MPC1/2*, *MCT1/4*, and *LDHa/b* in primary breast cancers (C) and lung metastases (M) from 4T1 mice (n = 7). Error bars denote SD.

(B–D) Relative metabolite levels in primary breast cancers (C) and lung metastases (M) from 4T1 mice (n = 4). Error bars denote SD. $^{**}p \leq 0.01$, $^{***}p \leq 0.005$ based on a two-tailed paired t test.

See also Figure S1.

Intracellular Pyruvate Levels and PC Expression Are Increased in Lung Metastases Compared to Primary Breast Cancers

Next, we sought to determine the mechanism by which the microenvironment regulates PC-dependent anaplerosis. Specifically, we investigated whether transcriptional and/or metabolic regulation of PC occurs in lung metastases compared to the primary breast cancers. We measured PC expression (transcriptional regulation) and pyruvate, glutamate, and α-ketoglutarate levels (metabolic regulation). We found that PC expression was increased in lung metastases compared to primary breast cancers (Figure 2A), which suggests a role for transcriptional regulation. The levels of glutamate and α-ketoglutarate, both known inhibitors of PC activity (Zeczycki et al., 2010), were respectively unaltered or showed an increasing trend in lung metastases (Figures 2B and 2C) and thus could not explain the increase in PC-dependent anaplerosis in lung metastases. Yet, pyruvate levels were increased in the lung metastases compared to the primary breast cancers, suggesting that they could contribute to increased PC activity (Figure 2D).

Next, we asked which alterations in metabolism resulted in increased pyruvate levels in lung metastases compared to the primary breast cancers. To answer this question, we measured gene expression patterns of enzymes and transporters downstream of pyruvate because decreased expression of any of them can result in increased pyruvate levels (Compan et al., 2015; Karlsson et al., 1974; Marchiq et al., 2015). Specifically, we tested whether the pyruvate-lactate-converting enzymes lactate dehydrogenase (LDH) a/b, the monocarboxylase transporters (MCT) 1/4 (that can transport lactate and pyruvate across the plasma membrane), and MPC1/2 (that transport pyruvate into the mitochondria) were differently expressed in lung metastases compared to the primary breast cancers (Figures 2E–2J). Surprisingly, we did not observe any significant decrease in the gene expression of these proteins. Yet, this finding was consistent with the fact that no lactate accumulation occurred in lung metastases compared to the primary breast cancers (Figure S1A). Therefore, we concluded that the increase in pyruvate levels within the lung metastases was not caused by decreased gene expression of pyruvate-converting or transporting proteins.

Pyruvate Addition to the Nutrient Microenvironment Increases Intracellular Pyruvate Levels and Modulates PC-Dependent Anaplerosis

Next, we investigated whether alterations in the nutrient microenvironment can result in similar metabolic changes to those we had observed in lung metastases compared to primary

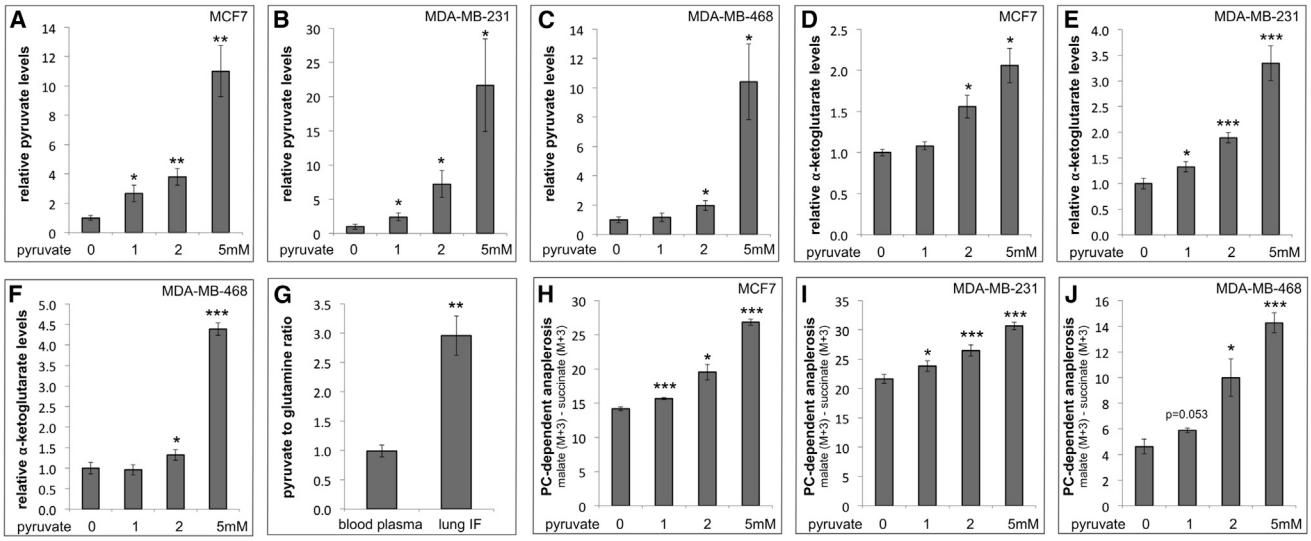

Figure 3. Pyruvate Addition to the Nutrient Microenvironment Increases Intracellular Pyruvate Levels and PC-Dependent Anaplerosis

(A–F) Pyruvate and α-ketoglutarate levels in breast cancer cell lines cultured with increasing amounts of pyruvate in the nutrient microenvironment ($n \geq 3$).

(G) Pyruvate to glutamine ratio in the interstitial fluid (IF) of the lungs and in blood plasma of healthy BALB/c mice ($n \geq 3$).

(H–J) Relative PC-dependent anaplerosis in breast cancer cell lines cultured with increasing amounts of pyruvate in the nutrient microenvironment (n = 3). Mass distribution vectors are provided in Table S2. Error bars denote SD. *$p \leq 0.05$, **$p \leq 0.01$, ***$p \leq 0.005$ based on a two-tailed paired t test.

See also Figures S1 and S2.

breast cancers. Interestingly, it has been shown that replacing glucose with pyruvate leads to increased intracellular pyruvate levels (Compan et al., 2015), yet this is not a physiological situation. Thus, we asked whether adding pyruvate in the presence of glucose to the in vitro nutrient microenvironment results in increased intracellular pyruvate levels. We found that addition of pyruvate resulted in increased intracellular pyruvate levels in three different breast cancer cell lines (MCF7, MDA-MB-231, and MDA-MB-468) (Figures 3A–3C). Moreover, lactate and glutamate levels did not increase upon addition of pyruvate to the nutrient microenvironment (Figures S1B–S1G), while α-ketoglutarate levels increased (Figures 3D–3F). Thus, pyruvate addition to the nutrient microenvironment resulted in similar metabolic changes than we had observed in lung metastases. This finding consequently indicates that lung metastases could exhibit increased intracellular pyruvate levels because of increased pyruvate availability in the lung microenvironment.

To test this possibility, we measured the pyruvate and glutamine levels in the lung interstitial fluid and compared them to those of blood plasma of healthy BALB/c mice. In line with our hypothesis that the lung in vivo microenvironment favors PC-dependent anaplerosis over glutamine anaplerosis, we found that the pyruvate/glutamine ratio was ~3-fold higher in the interstitial fluid of the lungs compared to the blood plasma (Figure 3G). This is in line with the observation that in lung tissue the protein expression of the pyruvate transporter SLC16A7 is >3-fold lower than the expression of the glutamine transporters SLC1A5 and SLC7A5 (Human Protein Atlas). Thus, these data indicate that the in vivo lung microenvironment favors PC-dependent anaplerosis in cancer cells because of pyruvate availability.

Next, we measured PC-dependent anaplerosis upon pyruvate addition to the nutrient microenvironment in the three breast cancer cell lines using $^{13}C_6$-glucose and $^{13}C_3$-pyruvate to correct for any label dilution resulting from pyruvate uptake. PC-dependent anaplerosis increased upon pyruvate addition to the nutrient microenvironment (Figures 3H–3J; Table S2), although neither *MPC1/2* expression nor *PC* expression was significantly increased (Figure S2). Notably, a 2-fold increase in intracellular pyruvate levels (that matched our measurements in lung metastases) resulted in increased PC-dependent anaplerosis in all three breast cancer cell lines, independently of their basal *PC* expression (that differed by >4.5-fold; data not shown). This argues that an increase in intracellular pyruvate levels can contribute to increased PC-dependent anaplerosis in breast cancer cells proliferating as lung metastases.

Neither the Cellular Acetyl-CoA Levels nor the ATP/ADP Ratio Are Altered upon Pyruvate Addition to the Nutrient Microenvironment

Next, we asked how increased pyruvate levels support PC-dependent anaplerosis. Several possible mechanisms have been described (Adina-Zada et al., 2012; Jitrapakdee et al., 2008; Taylor et al., 1969; von Glutz and Walter, 1976; Walter and Stucki, 1970): (1) pyruvate can stimulate an oxidative metabolism and increase the ATP/ADP ratio that in turn promotes PC activity; (2) pyruvate can increase levels of acetyl-CoA, which is a known allosteric activator of PC activity; and (3) pyruvate can promote PC activity via increased substrate availability and thus enzyme kinetics.

We tested whether any of the above mechanisms was responsible for the increased PC-dependent anaplerosis upon an

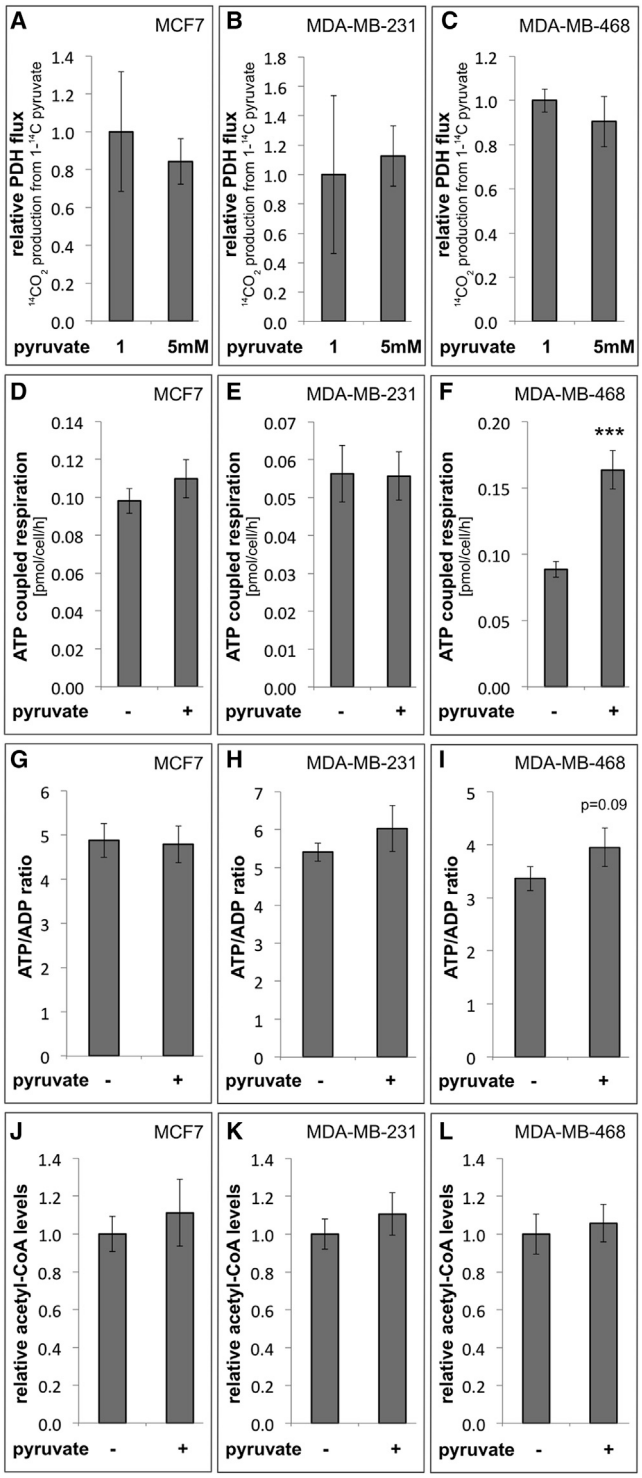

Figure 4. Neither the ATP/ADP Ratio nor Acetyl-CoA Levels Correlate with PC-Dependent Anaplerosis

(A–C) Relative PDH flux in breast cancer cell lines cultured with 1 or 5 mM of pyruvate in the nutrient microenvironment (n = 3). PDH flux was measured based on the normalized $^{14}CO_2$ production from 1-^{14}C-pyruvate.

(D–F) ATP-coupled respiration in breast cancer cell lines cultured with or without 5 mM of pyruvate in the nutrient microenvironment (n = 6). ATP-coupled respiration was assessed by the difference between total oxygen consumption rates and oxygen consumption rates in the presence of the ATP synthase inhibitor oligomycin A (1 μM).

(G–L) ATP/ADP ratio and acetyl-CoA levels in breast cancer cell lines cultured with or without 5 mM of pyruvate in the nutrient microenvironment (n = 3). Error bars denote SD. ***p ≤ 0.005 based on a two-tailed paired t test.

See also Figure S3.

increase in intracellular pyruvate levels. We measured the ATP/ADP ratio as well as the acetyl-CoA levels (using liquid chromatography mass spectrometry) and quantified oxidative TCA cycle metabolism based on ATP-coupled respiration (using a Clark electrode) as well as PDH flux (based on radioactive $^{14}CO_2$ capture from 1-^{14}C-pyruvate) in breast cancer cell lines upon pyruvate addition to the nutrient microenvironment. All these measurements were not significantly changed upon pyruvate addition to the nutrient microenvironment in the three cell lines (Figures 4A–4L). The only exception was ATP-coupled respiration in MDA-MB-468 cells, which increased upon pyruvate addition to the nutrient microenvironment and can be explained by increased NADH production via serine biosynthesis (Figure S3). Based on these measurements, we concluded that neither the cell average ATP/ADP ratio nor acetyl-CoA levels correlated with the relative changes in PC-dependent anaplerosis upon pyruvate addition to the nutrient microenvironment.

The Molar Distribution of Pyruvate between the Mitochondria and the Cytosol Can be Calculated Based on ^{13}C Labeling Data

Metabolite concentrations can alter metabolite conversion rates via enzyme kinetics as long as enzyme saturation is not reached (Fendt et al., 2010; Park et al., 2016). The metabolite concentration that leads to 50% enzyme saturation (assuming standard Michaelis-Menten kinetics) defines the so-called K_m value of an enzyme. Because PC is a mitochondrial enzyme, pyruvate concentration alterations within the mitochondria that are below or in the range of the K_m value for PC can promote PC-dependent anaplerosis via enzyme kinetics. To test for this possibility, we decided to investigate the compartment-specific distribution of pyruvate.

Standard metabolomics approaches can only report cell-average metabolite levels, because metabolites are extracted from the entire cell. Thus, the information on how much of a metabolite is located within different compartments such as the cytosol and the mitochondria is lost. Therefore, we decided to develop a mathematical model that allowed us to determine the molar amount of mitochondrial and cytosolic pyruvate based on ^{13}C labeling data.

The basis of this model is that conservation of mass applies when extracting a metabolite from a cell with different compartments (Figure 5A). The conservation of mass for the compartmentalized molar amounts of a metabolite reads:

$$n_{total} = \sum_{k=1}^{N} n_k \qquad \text{(Equation 1)}$$

Here, n_k is the molar amount of a metabolite in the compartment k, with k ranging from 1 to N, and n_{total} is the molar amount of that metabolite within the entire cell.

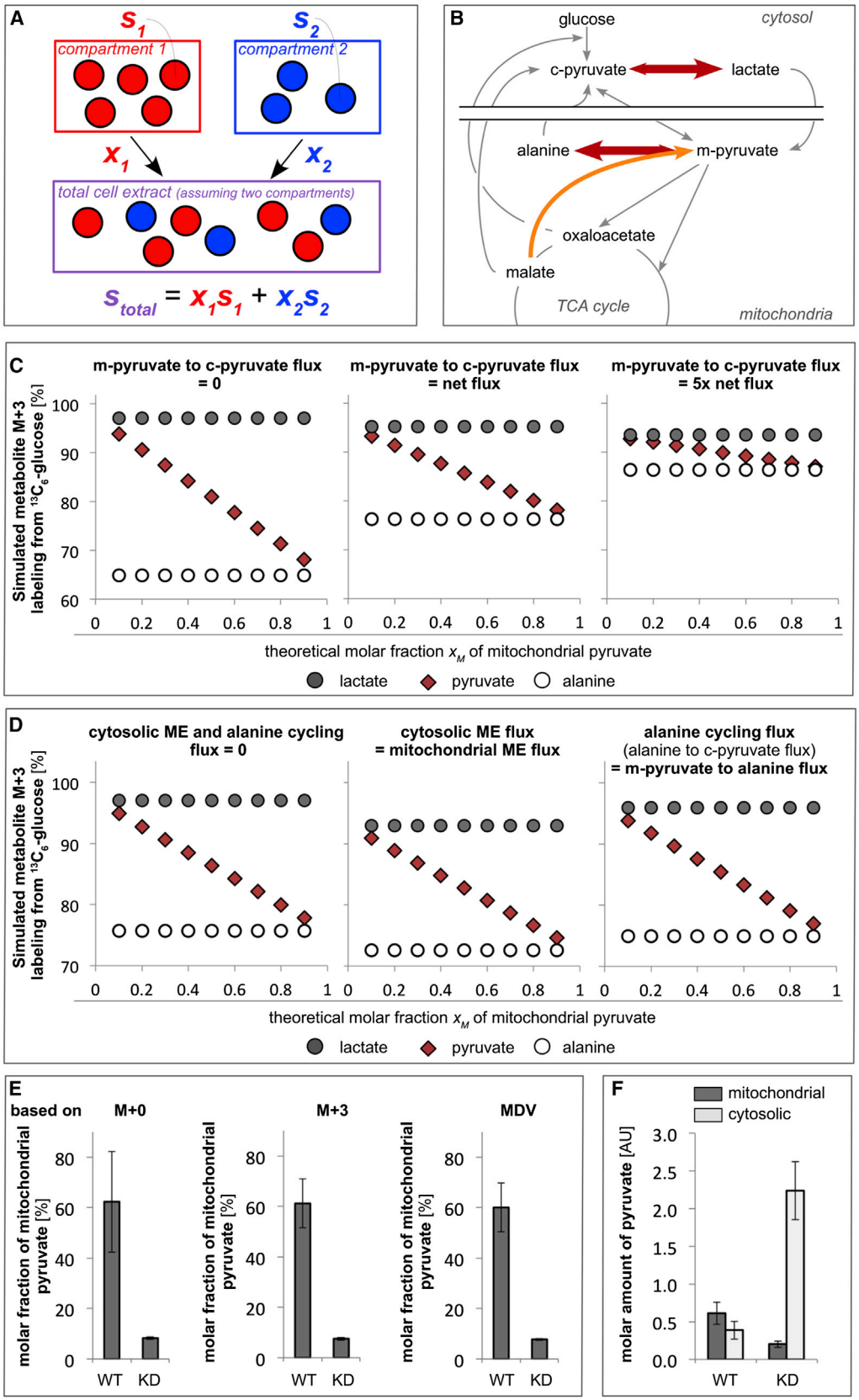

(legend on next page)

Moreover, we can further define the molar fraction x_k with which n_k (metabolite amount within compartment k) contributes to n_{total} (the amount of the same metabolite within the entire cell),

$$x_k = \frac{n_k}{n_{total}} \quad \text{(Equation 2)}$$

with

$$\sum_{k=1}^{N} x_k = 1 \quad \text{(Equation 3)}$$

Consequently, we can compute n_k from measured x_k and n_{total} as $n_k = x_k * n_{total}$.

With a standard metabolomics approach, we can estimate n_{total} based on the measurement of the amount of the same metabolite within the entire sample (n) and knowledge of the number of cells (Z) used to prepare the sample:

$$n_{total} = \frac{n}{Z} \quad \text{(Equation 4)}$$

Next, we assumed that each n_k is associated with a specific and known property s_k (e.g., a chemical difference such as a stable isotope enrichment pattern). Consequently, s_{total} consists of an average of these compartment-specific properties s_k, weighted by the fractional compartmental contribution x_k (Figure 5A),

$$s_{total} = \sum_{k=1}^{N} x_k * s_k \quad \text{(Equation 5)}$$

Thus, Equation 5 allows estimating x_k based on known s_k and measured s_{total}.

Stable isotope enrichment patterns of a metabolite can be used as s_k and s_{total} when the biochemical pathways by which that metabolite is produced differ between compartments:

$$s_k = MDV_k \quad \text{(Equation 6)}$$

and

$$s_{total} = MDV_{total} \quad \text{(Equation 7)}$$

Here, MDV is the mass distribution vector, which describes the fractional abundance of each isotopologue normalized with the sum of all possible isotopologues, and formally describes the measured labeling pattern.

Next, we specified our model for pyruvate (because it is our metabolite of interest) assuming ^{13}C as the stable isotope to generate compartment-specific stable isotope enrichments in pyruvate. To do so, we simplified Equations 2, 3, and 5 by assuming that pyruvate is only present in considerable amounts within the mitochondria and the cytosol. This assumption is based on the fact that the major pyruvate producing and converting enzymes (pyruvate kinase, lactate dehydrogenase, malic enzyme, pyruvate carboxylase, and pyruvate dehydrogenase) are located in these two compartments (Genecards database). Although some of these enzymes can also be located in the nucleus, small molecules such as metabolites and proteins below 40 kDa can freely diffuse through the nuclear pores (Strasser et al., 2012). Thus, the cytosolic metabolite pool is in complete exchange with the nuclear metabolite pool. Therefore, applying Equations 2, 3, 5, 6, and 7 to a two-compartment system (cytosol (C) and mitochondria (M)) leads to

$$MDV_{total} = x_M * MDV_M + x_C * MDV_C \quad \text{(Equation 8)}$$

and

$$x_M + x_C = 1 \quad \text{(Equation 9)}$$

Substituting $x_C = 1 - x_M$ from Equation 9 into Equation 8, results in

$$MDV_{total} = x_M * MDV_M + (1 - x_M) * MDV_C \quad \text{(Equation 10)}$$

Here, the MDV_{total} is given by the measurement of the ^{13}C labeling from pyruvate (MDV_P) when metabolites are extracted from the entire cell:

$$MDV_{total} = MDV_P \quad \text{(Equation 11)}$$

Figure 5. Compartment-Specific Molar Fractions of Pyruvate Can Be Determined Based on ^{13}C Labeling Patterns

(A) Conservation of mass applies when extracting a metabolite from a cell with different compartments. The metabolite of interest (in our case pyruvate) has in compartment 1 (red) the specific and known property s_1 (e.g., a stable isotope enrichment) and in compartment 2 (blue) the specific and known property s_2 (e.g., another stable isotope enrichment). Consequently, when assuming that only two compartments exist, then the property of the total cell extract s_{total} (purple) consists of a mix of the compartment-specific properties s_1 and s_2, weighted by the molar contributions x_1 of the metabolite from compartment 1 and x_2 of the metabolite from compartment 2.

(B) The mathematical model requires that lactate is produced from cytosolic (c) pyruvate and alanine from mitochondrial (m) pyruvate, and thus that the corresponding enzymatic reactions (red arrows) are compartment-specific. In this case, lactate reflects the ^{13}C labeling enrichment of cytosolic pyruvate and alanine the ^{13}C labeling enrichment of mitochondrial pyruvate. Moreover, a metabolic flux (e.g., mitochondrial malic enzyme flux) needs to exist that results in a mitochondrial-specific ^{13}C labeling enrichment of mitochondrial pyruvate (orange arrow). The presence of any flux that leads to exchange between cytosolic and mitochondrial pyruvate does not invalidate the mathematical model but can result in labeling differences between lactate and alanine that are too small to be measured reliably.

(C) Simulated M+3 labeling of lactate, pyruvate, and alanine against the theoretical molar fraction of mitochondrial pyruvate. Net flux was assumed to occur in forward direction (flux from cytosolic to mitochondrial pyruvate).

(D) Simulated M+3 labeling of lactate, pyruvate, and alanine against the theoretical molar fraction of mitochondrial pyruvate.

(E and F) Molar fraction of mitochondrial (m) and cytosolic (c) pyruvate estimated from a published dataset (Vacanti et al., 2014) comprising control cells (WT) and mitochondrial pyruvate carrier (MPC) knockdown (KD) cells. Lactate, pyruvate, and alanine M+0, M+3, or the total mass distribution vector (MDV) (using a least-squares fit) was used as input to our mathematical model. Molar amounts of mitochondrial and cytosolic pyruvate were based on the estimated molar fractions and the published total intracellular pyruvate levels. Error bars denote SE.

See also Figures S4, S5, and S6.

Similarly, $MDV_{M\text{-}P}$ and $MDV_{C\text{-}P}$ are the ^{13}C labeling patterns of mitochondrial and cytosolic pyruvate, respectively. However, we cannot directly measure $MDV_{M\text{-}P}$ and $MDV_{C\text{-}P}$, because we extract all metabolites of a cell regardless of which compartment they are located in. Thus, we screened for metabolites whose ^{13}C labeling patterns can be easily measured and that specifically reflect the ^{13}C labeling patterns of mitochondrial and cytosolic pyruvate. Such metabolites, which we called reporter metabolites, need to fulfill the following prerequisites: (1) they are produced from either cytosolic or mitochondrial pyruvate by compartment-specific enzymes, (2) they may not be produced from any metabolite other than pyruvate, and they should not be in the media composition, and (3) their ^{13}C labeling patterns must reflect the respective compartment–specific labeling patterns of pyruvate. Notably, if (1) and (2) are fulfilled, then (3) is automatically satisfied as long as stable isotope enrichment (labeling) steady state has been reached. However, (3) might not be fulfilled during the dynamic ^{13}C enrichment phase. This is because ^{13}C enrichment dynamics are a function of time as well as of the fluxes and metabolite pool sizes present between the labeled substrate, the metabolite of interest, and the reporter metabolites (Buescher et al., 2015).

Lactate and alanine have the potential to fulfill both prerequisites in in vitro culture conditions (notably, neither lactate nor alanine fulfill prerequisite (2) in vivo, because both metabolites are found within the blood, and thus need to be considered to be part of the media composition) (Figure 5B). Lactate and alanine are neither in the DMEM formulation nor in dialyzed serum. Moreover, lactate is produced from cytosolic pyruvate, and there is strong evidence that alanine is predominantly produced from mitochondrial pyruvate (Vacanti et al., 2014; Yang et al., 2014). We verified the latter assumption for MCF7, MDA-MB-231, and MDA-MB-468 cell lines (Figure S4). One additional possibility is that alanine is not synthesized de novo, but derived from protein breakdown. We experimentally excluded this possibility for MCF7, MDA-MB-231, and MDA-MB-468 cell lines (Figure S5). Thus, under the prerequisite that cytosolic alanine aminotransferase flux (compared to mitochondrial alanine aminotransferase flux) and protein breakdown are marginal or not present, we can assume in steady state that the labeling patterns of alanine (MDV_A) reflect those of mitochondrial pyruvate ($MDV_{M\text{-}P}$), while the labeling patterns of lactate (MDV_L) reflect those of cytosolic pyruvate ($MDV_{C\text{-}P}$):

$$MDV_{M-P} = MDV_A \quad \text{(Equation 12)}$$

and

$$MDV_{C-P} = MDV_L \quad \text{(Equation 13)}$$

Combining Equations 10, 11, 12, and 13, we formulate that x_M is a function of the cell average ^{13}C labeling patterns measured in pyruvate, alanine, and lactate:

$$MDV_P = x_M * MDV_A + (1 - x_M) * MDV_L \quad \text{(Equation 14)}$$

and

$$x_M = \frac{MDV_P - MDV_L}{MDV_A - MDV_L} \quad \text{(Equation 15)}$$

By combining Equations 2, 9, and 15, we can calculate the molar amount of pyruvate within the cytosol ($n_{C\text{-}P}$) and within the mitochondria ($n_{M\text{-}P}$), as:

$$n_{M-P} = x_M * n_P \quad \text{(Equation 16)}$$

and

$$n_{C-P} = (1 - x_M) * n_P \quad \text{(Equation 17)}$$

Here, n_P denotes the total molar pyruvate amount of the entire cell.

As indicated earlier (and also evidenced by Equation 15), to obtain a valid solution from Equation 15, the ^{13}C labeling patterns of mitochondrial and cytosolic pyruvate, and thus those of alanine and lactate, need to differ. Biologically, this means that mitochondrial pyruvate needs to be produced not only from cytosolic pyruvate, but in addition by another biochemical pathway that alters the ^{13}C labeling pattern of mitochondrial pyruvate and thus alanine (Figure 5B). This requires mitochondrial malic enzyme (ME) flux. Notably, mitochondrial phosphoenolpyruvate carboxykinase (PCK) activity combined with mitochondrial pyruvate kinase activity would have a similar effect as mitochondrial ME flux. Yet, activity of cytosolic ME, cytosolic PCK, alanine cycling, as well as exchange flux between mitochondrial and cytosolic pyruvate, all decrease the difference between ^{13}C labeling patterns of mitochondrial and cytosolic pyruvate, and thus those of alanine and lactate. To quantify the influence of these fluxes on the ^{13}C labeling of pyruvate, alanine, and lactate, we used a flux model (see the Supplemental Experimental Procedures) and simulated the MDVs of pyruvate, lactate, and alanine based on theoretical flux solutions using the MATLAB-based software, Metran (Antoniewicz et al., 2007). Within the theoretical flux solutions, we tested (1) alterations in exchange flux between mitochondrial and cytosolic pyruvate, (2) alterations in cytosolic ME flux (that has the same effect as cytosolic PCK flux), and (2) alterations in alanine cycling (Table S3). We found that increased exchange flux between mitochondrial and cytosolic pyruvate (but not cytosolic lactate dehydrogenase or mitochondrial alanine aminotransferase exchange flux) decreased the difference between the ^{13}C labeling patterns of alanine and lactate (Figure 5C; Table S3). The effect of cytosolic ME flux and alanine cycling on the difference between the ^{13}C labeling patterns of alanine and lactate was much less pronounced than that of pyruvate exchange flux (Figure 5D; Table S3). This is because ME and alanine cycling flux are small compared to the glycolytic flux toward cytosolic pyruvate. Notably, the validity of Equation 15 did not depend on the presence or absence of pyruvate exchange, cytosolic ME flux, alanine cycling, or PC flux (Figures 5B–5D; Table S3). Equation 15 only fails if the ^{13}C labeling patterns of alanine and lactate are identical. Thus, as long as there is a sufficient mitochondrial ME flux, the accuracy of the results obtained from Equation 15 only depends on measurement accuracy.

Next, we tested whether measured data would allow solving Equation 15. Because a standard gas chromatograph-mass spectrometer has a measurement precision of $\sim\pm1\%$, we argued that we need at least an absolute difference of 2% in the labeling of lactate and alanine to solve Equation 15 reliably.

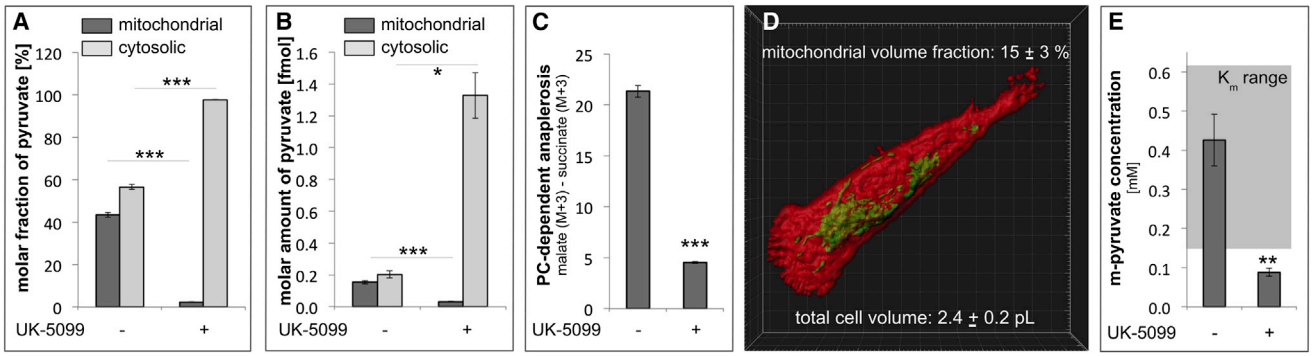

Figure 6. The Mitochondrial Pyruvate Concentration Correlates with PC-Dependent Anaplerosis and Is in the K_m Range for PC

(A and B) Molar fraction and molar amount of cytosolic pyruvate in MDA-MB-231 cells treated with and without the mitochondrial pyruvate carrier (MPC) inhibitor UK-5099 (10 μM) ($n \geq 3$), estimated based on our mathematical model. Mass distribution vectors are provided in Table S5. Error bars depict SE.

(C) PC-dependent anaplerosis in MDA-MB-231 cells treated with and without the mitochondrial pyruvate carrier (MPC) inhibitor UK-5099 (10 μM) ($n \geq 3$). Mass distribution vectors are provided in Table S5. Error bars depict SD.

(D) Representative picture of the 3D cellular reconstruction based on immunofluorescence staining. Plasma membrane and mitochondria are depicted in red and green, respectively. Total cell volume was measured with an automated cell counter. Error range represents SD.

(E) Mitochondrial (m) pyruvate concentration in MDA-MB-231 cells estimated based on our mathematical model and the experimental determination of the mitochondrial cell volume with and without treatment of the mitochondrial pyruvate carrier (MPC) inhibitor UK-5099 (10 μM) ($n \geq 3$). Error bars depict SD. Grey area highlights published K_m value range of pyruvate for PC. *$p \leq 0.05$, **$p \leq 0.01$, ***$p \leq 0.005$ based on a two-tailed paired t test.

See also Figure S6.

We used a published ^{13}C labeling dataset from mitochondrial pyruvate carrier (MPC) knockdown and control C2C12 myoblasts (Vacanti et al., 2014) (Table S4) as input (M+0, M+3, or entire MDVs) to our mathematical model. Corroborating our hypothesis that measured data are sufficient in their accuracy to solve Equation 15, we found that MPC knockdown decreased the mitochondrial fraction of pyruvate by ~8-fold (Figure 5E). Because the results obtained using different inputs (M+0, M+3, or entire MDVs) to Equation 15 were all very similar, we decided to always use the fit of the entire MDVs because this takes all isotopologues for each metabolite into account. Thus, we next calculated the molar mitochondrial and cytosolic amount of pyruvate based on Equations 16 and 17, which confirmed that the total molar pyruvate amount in the mitochondria decreased upon MPC knockdown (Figure 5F). Thus, this test shows that we can resolve the compartment-specific molar pyruvate amounts in the mitochondria and the cytosol based on our mathematical model and measured cell average ^{13}C labeling patterns.

Next, we used the developed model to calculate the molar amount of mitochondrial pyruvate in MDA-MB-231 cells (that showed sufficient labeling difference in alanine and lactate) in the presence and absence of the mitochondrial pyruvate carrier inhibitor UK-5099. Using this pharmacological inhibitor, we expected reduced molar amount of pyruvate in the mitochondria and consequently reduced PC-dependent anaplerosis (Table S5). Indeed, we found that the mitochondrial pyruvate fraction and the molar amount of mitochondrial pyruvate decreased upon treatment with UK-5099 (Figures 6A and 6B). To corroborate our overall findings, we next measured PC-dependent anaplerosis in the presence and absence of UK-5099. As expected from our findings, we found that PC-dependent anaplerosis decreased upon UK-5099 treatment (Figure 6C). Thus, we concluded that mitochondrial pyruvate is relevant for altering PC-dependent anaplerosis and this happens likely via enzyme kinetics.

Mitochondrial Pyruvate Concentrations Are in the K_m Range for Pyruvate Carboxylase

To finally prove that altered pyruvate levels promote PC-dependent anaplerosis via enzyme kinetics, we estimated the mitochondrial pyruvate concentration in MDA-MB-231 cells and compared it to the K_m of PC for pyruvate. Based on the molar amount of pyruvate within the mitochondria ($n_{M\text{-}P}$), the actual mitochondrial pyruvate concentration ($c_{M\text{-}P}$) can be determined by estimating the cytosolic ($V_{C\text{-}P}$) and the mitochondrial ($V_{M\text{-}P}$) cell volume:

$$c_{M-P} = \frac{n_{M-P}}{V_{M-P}} \qquad \text{(Equation 18)}$$

To assess mitochondrial cell volume, we performed an immunofluorescence staining of the plasma membrane and the mitochondria. Subsequently, we acquired confocal image scans and performed a three-dimensional (3D) cell reconstruction, which allowed us to estimate the mitochondrial volume fraction in MDA-MB-231 cells (Figure 6D). Next, we measured the total cell volume using a MOXI Z Mini Automated Cell Counter (ORFLO). The measured total cell volume was multiplied with the estimated mitochondrial volume fraction, resulting in an estimate of the mitochondrial cell volume. Based on these measurements, we estimated the mitochondrial pyruvate concentration in MDA-MB-231 cells and compared it to the published K_m value range of 0.15–0.62 mM (McClure et al., 1971; Scrutton and White, 1974; Taylor et al., 1969). The estimated mitochondrial pyruvate concentration was 0.42 mM, which is within in the range of the K_m values from literature (Figure 6E). Accordingly, upon treatment with UK-5099, the mitochondrial

pyruvate concentration dropped below the K_m value range (Figure 6E). Thus, we concluded that alterations in mitochondrial pyruvate concentration can directly translate into increased PC-dependent anaplerosis via enzyme kinetics and consequently can contribute to increased PC-dependent anaplerosis in lung metastases.

DISCUSSION

Here, we discovered that breast cancer cells proliferating as lung metastases increase PC-dependent anaplerosis as a result of a change in the in vivo microenvironment. Based on the developed mathematical model that we used to determine mitochondrial pyruvate concentrations, we provide evidence for a role of metabolic regulation in this process.

Recently, it has been described that switching cells from an in vitro to an in vivo microenvironment promotes PC-dependent anaplerosis via regulation at the expression level (Davidson et al., 2016). Beyond this finding, we show that changes within the in vivo microenvironment can result in increased PC-dependent anaplerosis. Similar to the above-mentioned study, we observed a role for transcriptional regulation in this process. Yet, we provide evidence for a combined transcriptional and metabolic regulation resulting in increased PC-dependent anaplerosis. This discovery adds to the increasing evidence of metabolic regulation, via metabolite concentrations or metabolite ratios, as an important regulatory mechanism within cells (Lorendeau et al., 2015). Moreover, our data imply that the organ-specific in vivo availability of nutrients, such as pyruvate, can promote PC-dependent anaplerosis. Consequently, susceptibility of cancers to metabolic drugs such as glutamine anaplerosis inhibitors (currently in clinical trial) (Elia et al., 2016) might be a function of the in vivo microenvironment. In support of this hypothesis, we found that not only increased *PC* expression is sufficient to render cells insensitive to glutamine anaplerosis inhibition (Cheng et al., 2011), but also that simply adding pyruvate to the nutrient microenvironment rescues the proliferation defect of glutamine anaplerosis inhibitor treated breast cancer cells (Figures S6A and S6B). Thus, the link between metabolism and the nutrient microenvironment needs to be considered to select effective metabolism-based therapies against cancers.

The genetic landscape and the cell origin are known modulators of cellular metabolism (Davidson et al., 2016; Elia et al., 2016; Yuneva et al., 2012). Yet, whether the in vivo microenvironment can modulate the metabolism of metastasizing cancers is poorly defined (Chen et al., 2015; Maher et al., 2012). By studying in vivo primary cancers and their corresponding metastases (i.e., cancers with the same cell origin proliferating in two different organs), we show that at least PC-dependent anaplerosis is a function of the organ-specific microenvironment. Our finding is thereby supported by the observation that breast cancer cells isolated from lung metastases of the 4T1 mouse model have a similar low PC-dependent anaplerosis as the parental 4T1 breast cancer cell line when cultured in the same in vitro microenvironment (Dupuy et al., 2015).

PC-dependent anaplerosis is mainly fueled by glycolytic carbon and therefore depends on MPC activity. However, many cancers show decreased MPC expression (Schell et al., 2014). Considering this observation and the data we provide, it can be speculated that the combination of MPC expression and pyruvate concentrations available in the microenvironment define the in vivo dependency of cancer cells on PC-dependent anaplerosis. In contrast with two recent publications (Compan et al., 2015; Schell et al., 2014), we found that activation of MPC activity with pyruvate does not necessarily result in increased ATP-coupled respiration. This difference can be explained by the fact that in both other studies, pyruvate was the sole glycolytic carbon source provided to the cancer cells, while we provided pyruvate on top of glucose. Consequently, in our setting, glycolysis can still be used to provide ATP, while this is not possible when pyruvate is the sole carbon source entering glycolysis. Thus, this indicates that pyruvate availability in the nutrient microenvironment can have a pro-proliferative role by supporting anaplerosis without increasing oxidative metabolism in the mitochondria.

Finally, we developed a mathematical model that allows the determination of the compartment-specific molar amounts of pyruvate from ^{13}C labeling and metabolomics data. Our method is complementary to the available fluorescence energy resonance transfer (FRET) sensor for pyruvate (San Martín et al., 2013), because, differently to the FRET sensor, we can simultaneously determine the cytosolic and mitochondrial pyruvate concentration during cellular steady state, while the FRET sensor is suitable to measure dynamic changes in cytosolic pyruvate upon short-term stimulation. Notably, our mathematical model can be used in other in vitro cultured cells as long as valid reporter metabolites for pyruvate in the tested cells exist. Moreover, it is possible to translate our mathematical model beyond pyruvate by combining it with genetic engineering of reporter metabolites. As a proof of concept, we showed that compartment-specific α-ketoglutarate levels can be determined with our mathematical model based on engineered reporter metabolites (Figures S6C–S6G; Table S6). This shows that our model can be combined with metabolic engineering to infer the compartment-specific distribution of metabolites for which no natural sensor metabolites exist.

EXPERIMENTAL PROCEDURES

Mathematical Model

The derivation and assumptions of the mathematical model are given in the Results. Notably, the mathematical model can only be applied in vitro, because in vivo both alanine and lactate are in the blood, and thus the prerequisite that both metabolites are only produced de novo from pyruvate fails. For each cell line, we tested the assumption that cytosolic alanine aminotransferase flux producing alanine is marginal or not present (Figure S4). The overdetermined equation system resulting from the MDVs was solved using the MATLAB build-in function *lscov*, which returns the ordinary least-squares solution and SE to a linear system of equations. All least-squares solutions are based on the simultaneous fit of labeling patterns from at least three biological replicates.

Cell Culture Conditions

All cell lines (MCF7, MDA-MB-231, and MDA-MB-468) were cultured in DMEM without pyruvate containing 10% dialyzed FBS and 1% penicillin/streptomycin and tested to be mycoplasma free. The media was replaced every 24 hr. Additional nutrients (^{13}C-labeled or ^{13}C-unlabeled) or drugs (UK-5099,10 μM; Sigma-Aldrich) were added 24 hr prior to cell harvest. CB839 (Calithera) was applied for 72 hr at a concentration of 200 nM.

^{13}C Tracer Analysis

^{13}C tracer analysis has been performed as described before (Fendt et al., 2013a, 2013b). See also the Supplemental Experimental Procedures.

PDH Flux

The decarboxylation of pyruvate was assessed using 1-^{14}C-pyruvate. See also the Supplemental Experimental Procedures.

Mouse Models and In Vivo ^{13}C Tracer Analysis

The 4T1 breast cancer mouse model was used, and in vivo ^{13}C tracer analysis was performed as described previously (Davidson et al., 2016; Quaegebeur et al., 2016). All animal experiments were approved by the ethics committee of KU Leuven.

Statistical Analysis

Statistical analysis was performed for each experiment on $n \geq 3$ biological replicates using a two-tailed paired t test. Either SEs or SDs were calculated as indicated in each figure legend.

SUPPLEMENTAL INFORMATION

Supplemental Information includes Supplemental Experimental Procedures, six figures, and six tables and can be found with this article online at http://dx.doi.org/10.1016/j.celrep.2016.09.042.

AUTHOR CONTRIBUTIONS

Investigation, S.C., D.L., D.B., R.S., K.M., K.V., and I.E.; Formal Analysis, S.C., D.L. J.M.B., M.F.O., T.G.P.G., K.D.B., and S.-M.F.; Methodology, S.-M.F.; Resource, S.M.D.; Writing – Original Draft, S.-M.F.; Writing – Review & Editing, S.C., D.L, T.G.P.G., and K.D.B.; Conceptualization and Supervision, S.-M.F. All authors have read and approved the manuscript.

ACKNOWLEDGMENTS

We thank Prof. Metallo (UCSD) for providing raw data to their MPC publication; Prof. Mazzone and Mr. Bieniasz-Krzywiec (VIB) as well as Dr. Ghesquière (VIB) for advice on the 4T1 model and acetyl-CoA measurements, respectively; Prof. Vander Heiden (MIT) for providing the IDH mutant plasmids; and the VIB Bio Imaging Core for advice. D.L. is recipient of a VIB-Marie Curie fellowship. T.G.P.G. is supported by WiFoMed, the Daimler and Benz Foundation in cooperation with the Reinhard Frank Foundation, the Bettina-Bräu-Foundation, the Kind-Philipp-Foundation, the "Deutsche Stiftung für junge Erwachsene mit Krebs," the Fritz-Thyssen Foundation (FTF-40.15.0.030MN), the Friedrich-Baur Foundation, and by the German Cancer Aid (DKH-111886 and DKH-70112257). S.-M.F. acknowledges funding support from Marie Curie-CIG, FWO-Odysseus II, Concern Foundation, FWO-Research Grants, KU-Leuven Methusalem co-funding, Eugène Yourassowsky Schenking, and Bayer Health Care.

Received: January 14, 2016
Revised: August 30, 2016
Accepted: September 14, 2016
Published: October 11, 2016

REFERENCES

Adina-Zada, A., Zeczycki, T.N., and Attwood, P.V. (2012). Regulation of the structure and activity of pyruvate carboxylase by acetyl CoA. Arch. Biochem. Biophys. *519*, 118–130.

Antoniewicz, M.R., Kelleher, J.K., and Stephanopoulos, G. (2007). Elementary metabolite units (EMU): a novel framework for modeling isotopic distributions. Metab. Eng. *9*, 68–86.

Boonsaen, T., Rojvirat, P., Surinya, K.H., Wallace, J.C., and Jitrapakdee, S. (2007). Transcriptional regulation of the distal promoter of the rat pyruvate carboxylase gene by hepatocyte nuclear factor 3β/Foxa2 and upstream stimulatory factors in insulinoma cells. Biochem. J. *405*, 359–367.

Buescher, J.M., Antoniewicz, M.R., Boros, L.G., Burgess, S.C., Brunengraber, H., Clish, C.B., DeBerardinis, R.J., Feron, O., Frezza, C., Ghesquiere, B., et al. (2015). A roadmap for interpreting (^{13})C metabolite labeling patterns from cells. Curr. Opin. Biotechnol. *34*, 189–201.

Chen, J., Lee, H.-J., Wu, X., Huo, L., Kim, S.-J., Xu, L., Wang, Y., He, J., Bollu, L.R., Gao, G., et al. (2015). Gain of glucose-independent growth upon metastasis of breast cancer cells to the brain. Cancer Res. *75*, 554–565.

Cheng, T., Sudderth, J., Yang, C., Mullen, A.R., Jin, E.S., Matés, J.M., and DeBerardinis, R.J. (2011). Pyruvate carboxylase is required for glutamine-independent growth of tumor cells. Proc. Natl. Acad. Sci. USA *108*, 8674–8679.

Compan, V., Pierredon, S., Vanderperre, B., Krznar, P., Marchiq, I., Zamboni, N., Pouyssegur, J., and Martinou, J.-C. (2015). Monitoring mitochondrial pyruvate carrier activity in real time using a BRET-based biosensor: investigation of the Warburg effect. Mol. Cell *59*, 491–501.

Davidson, S.M., Papagiannakopoulos, T., Olenchock, B.A., Heyman, J.E., Keibler, M.A., Luengo, A., Bauer, M.R., Jha, A.K., O'Brien, J.P., Pierce, K.A., et al. (2016). Environment impacts the metabolic dependencies of ras-driven non-small cell lung cancer. Cell Metab. *23*, 517–528.

Deberardinis, R.J., Sayed, N., Ditsworth, D., and Thompson, C.B. (2008). Brick by brick: metabolism and tumor cell growth. Curr. Opin. Genet. Dev. *18*, 54–61.

Dupuy, F., Tabariès, S., Andrzejewski, S., Dong, Z., Blagih, J., Annis, M.G., Omeroglu, A., Gao, D., Leung, S., Amir, E., et al. (2015). PDK1-dependent metabolic reprogramming dictates metastatic potential in breast cancer. Cell Metab. *22*, 577–589.

Elia, I., Schmieder, R., Christen, S., and Fendt, S.-M. (2016). Organ-specific cancer metabolism and its potential for therapy. Handbook Exp. Pharmacol. *233*, 321–353.

Fan, T.W.M., Lane, A.N., Higashi, R.M., Farag, M.A., Gao, H., Bousamra, M., and Miller, D.M. (2009). Altered regulation of metabolic pathways in human lung cancer discerned by (13)C stable isotope-resolved metabolomics (SIRM). Mol. Cancer *8*, 41.

Fendt, S.M., Buescher, J.M., Rudroff, F., Picotti, P., Zamboni, N., and Sauer, U. (2010). Tradeoff between enzyme and metabolite efficiency maintains metabolic homeostasis upon perturbations in enzyme capacity. Mol. Syst. Biol. *6*, 356.

Fendt, S.M., Bell, E.L., Keibler, M.A., Davidson, S.M., Wirth, G.J., Fiske, B., Mayers, J.R., Schwab, M., Bellinger, G., Csibi, A., et al. (2013a). Metformin decreases glucose oxidation and increases the dependency of prostate cancer cells on reductive glutamine metabolism. Cancer Res. *73*, 4429–4438.

Fendt, S.M., Bell, E.L., Keibler, M.A., Olenchock, B.A., Mayers, J.R., Wasylenko, T.M., Vokes, N.I., Guarente, L., Vander Heiden, M.G., and Stephanopoulos, G. (2013b). Reductive glutamine metabolism is a function of the α-ketoglutarate to citrate ratio in cells. Nat. Commun. *4*, 2236.

Hensley, C.T., Faubert, B., Yuan, Q., Lev-Cohain, N., Jin, E., Kim, J., Jiang, L., Ko, B., Skelton, R., Loudat, L., et al. (2016). Metabolic heterogeneity in human lung tumors. Cell *164*, 681–694.

Jitrapakdee, S., St. Maurice, M., Rayment, I., Cleland, W.W., Wallace, J.C., and Attwood, P.V. (2008). Structure, mechanism and regulation of pyruvate carboxylase. Biochem. J. *413*, 369–387.

Karlsson, J., Hultén, B., and Sjödin, B. (1974). Substrate activation and product inhibition of LDH activity in human skeletal muscle. Acta Physiol. Scand. *92*, 21–26.

Lorendeau, D., Christen, S., Rinaldi, G., and Fendt, S.-M. (2015). Metabolic control of signalling pathways and metabolic auto-regulation. Biol. Cell *107*, 251–272.

Maher, E.A., Marin-Valencia, I., Bachoo, R.M., Mashimo, T., Raisanen, J., Hatanpaa, K.J., Jindal, A., Jeffrey, F.M., Choi, C., Madden, C., et al. (2012). Metabolism of [U-13 C]glucose in human brain tumors in vivo. NMR Biomed. *25*, 1234–1244.

Marchiq, I., Le Floch, R., Roux, D., Simon, M.-P., and Pouyssegur, J. (2015). Genetic disruption of lactate/H+ symporters (MCTs) and their subunit

CD147/BASIGIN sensitizes glycolytic tumor cells to phenformin. Cancer Res. *75*, 171–180.

McClure, W.R., Lardy, H.A., Wagner, M., and Cleland, W.W. (1971). Rat liver pyruvate carboxylase. II. Kinetic studies of the forward reaction. J. Biol. Chem. *246*, 3579–3583.

Park, J.O., Rubin, S.A., Xu, Y.-F., Amador-Noguez, D., Fan, J., Shlomi, T., and Rabinowitz, J.D. (2016). Metabolite concentrations, fluxes and free energies imply efficient enzyme usage. Nat. Chem. Biol. *12*, 482–489.

Pavlova, N.N., and Thompson, C.B. (2016). The emerging hallmarks of cancer metabolism. Cell Metab. *23*, 27–47.

Quaegebeur, A., Segura, I., Schmieder, R., Verdegem, D., Decimo, I., Bifari, F., Dresselaers, T., Eelen, G., Ghosh, D., Davidson, S.M., et al. (2016). Deletion or inhibition of the oxygen sensor PHD1 protects against ischemic stroke via reprogramming of neuronal metabolism. Cell Metab. *23*, 280–291.

San Martín, A., Ceballo, S., Ruminot, I., Lerchundi, R., Frommer, W.B., and Barros, L.F. (2013). A genetically encoded FRET lactate sensor and its use to detect the Warburg effect in single cancer cells. PLoS ONE *8*, e57712.

Schell, J.C., Olson, K.A., Jiang, L., Hawkins, A.J., Van Vranken, J.G., Xie, J., Egnatchik, R.A., Earl, E.G., DeBerardinis, R.J., and Rutter, J. (2014). A role for the mitochondrial pyruvate carrier as a repressor of the Warburg effect and colon cancer cell growth. Mol. Cell *56*, 400–413.

Scrutton, M.C., and White, M.D. (1974). Prufication and properties of human liver pyruvate carboxylase. Biochem. Med. *9*, 217–292.

Sellers, K., Fox, M.P., Bousamra, M., 2nd, Slone, S.P., Higashi, R.M., Miller, D.M., Wang, Y., Yan, J., Yuneva, M.O., Deshpande, R., et al. (2015). Pyruvate carboxylase is critical for non-small-cell lung cancer proliferation. J. Clin. Invest. *125*, 687–698.

Strasser, C., Grote, P., Schäuble, K., Ganz, M., and Ferrando-May, E. (2012). Regulation of nuclear envelope permeability in cell death and survival. Nucleus *3*, 540–551.

Taylor, H., Nielsen, J., and Keech, D.B. (1969). Substrate activation of pyruvate carboxylase by pyruvate. Biochem. Biophys. Res. Commun. *37*, 723–728.

Vacanti, N.M., Divakaruni, A.S., Green, C.R., Parker, S.J., Henry, R.R., Ciaraldi, T.P., Murphy, A.N., and Metallo, C.M. (2014). Regulation of substrate utilization by the mitochondrial pyruvate carrier. Mol. Cell *56*, 425–435.

Vanderperre, B., Bender, T., Kunji, E.R.S., and Martinou, J.-C. (2015). Mitochondrial pyruvate import and its effects on homeostasis. Curr. Opin. Cell Biol. *33*, 35–41.

von Glutz, G., and Walter, P. (1976). Regulation of pyruvate carboxylation by acetyl-CoA in rat liver mitochondria. FEBS Lett. *72*, 299–303.

Walter, P., and Stucki, J.W. (1970). Regulation of pyruvate carboxylase in rat liver mitochondria by adenine nucleotides and short chain fatty acids. Eur J Biochem. *12*, 508–519.

Yang, C., Ko, B., Hensley, C.T., Jiang, L., Wasti, A.T., Kim, J., Sudderth, J., Calvaruso, M.A., Lumata, L., Mitsche, M., et al. (2014). Glutamine oxidation maintains the TCA cycle and cell survival during impaired mitochondrial pyruvate transport. Mol. Cell *56*, 414–424.

Yuneva, M.O., Fan, T.W., Allen, T.D., Higashi, R.M., Ferraris, D.V., Tsukamoto, T., Matés, J.M., Alonso, F.J., Wang, C., Seo, Y., et al. (2012). The metabolic profile of tumors depends on both the responsible genetic lesion and tissue type. Cell Metab. *15*, 157–170.

Zeczycki, T.N., Maurice, M.S., and Attwood, P.V. (2010). Inhibitors of pyruvate carboxylase. Open Enzyme Inhib. J. *3*, 8–26.

Cell Reports, Volume *17*

Supplemental Information

Breast Cancer-Derived Lung Metastases Show Increased Pyruvate Carboxylase-Dependent Anaplerosis

Stefan Christen, Doriane Lorendeau, Roberta Schmieder, Dorien Broekaert, Kristine Metzger, Koen Veys, Ilaria Elia, Joerg Martin Buescher, Martin Franz Orth, Shawn Michael Davidson, Thomas Georg Philipp Grünewald, Katrien De Bock, and Sarah-Maria Fendt

Supplement

Christen *et al.*: Breast cancer-derived lung metastases show increased pyruvate carboxylase-dependent anaplerosis

Figures S1-S6

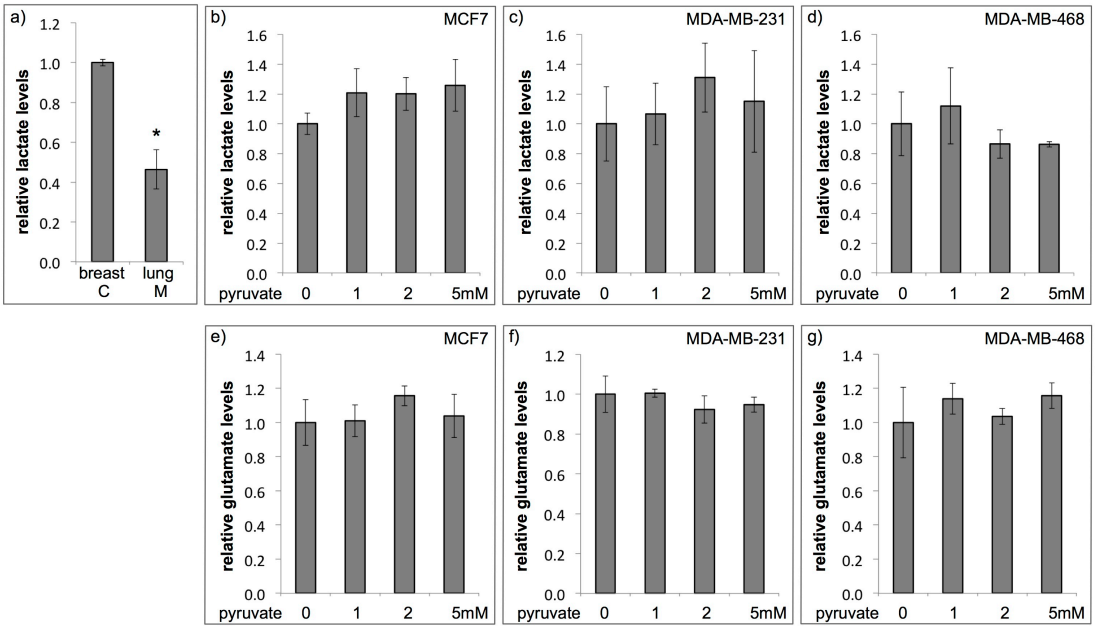

Figure S1: Metabolite levels of lung metastases, primary breast tumors, and breast cancer cell lines with and without pyruvate addition to the microenvironment. *Related to Figure 2 and 3.*

a) Relative lactate levels in primary breast cancers (C) and lung metastases (M) from 4T1 mice (n=4). Lactate levels were normalized to tissue weight and represented as fold change compared to the primary breast cancers. Error bars depict standard error. b-g) Metabolite levels in breast cancer cell lines upon pyruvate addition to the nutrient microenvironment. Relative change in lactate (b-d) and glutamate (e-g) levels after 24h of pyruvate (0-5mM) addition to the nutrient microenvironment in MCF7, MDA-MB-231, and MDA-MB-468 breast cancer cell lines (n=3). Metabolite levels were normalized to cell number and represented as fold change compared to the no-pyruvate condition. Error bars depict standard deviation. * indicates $p \leq 0.05$ based on a two-tailed paired t-test.

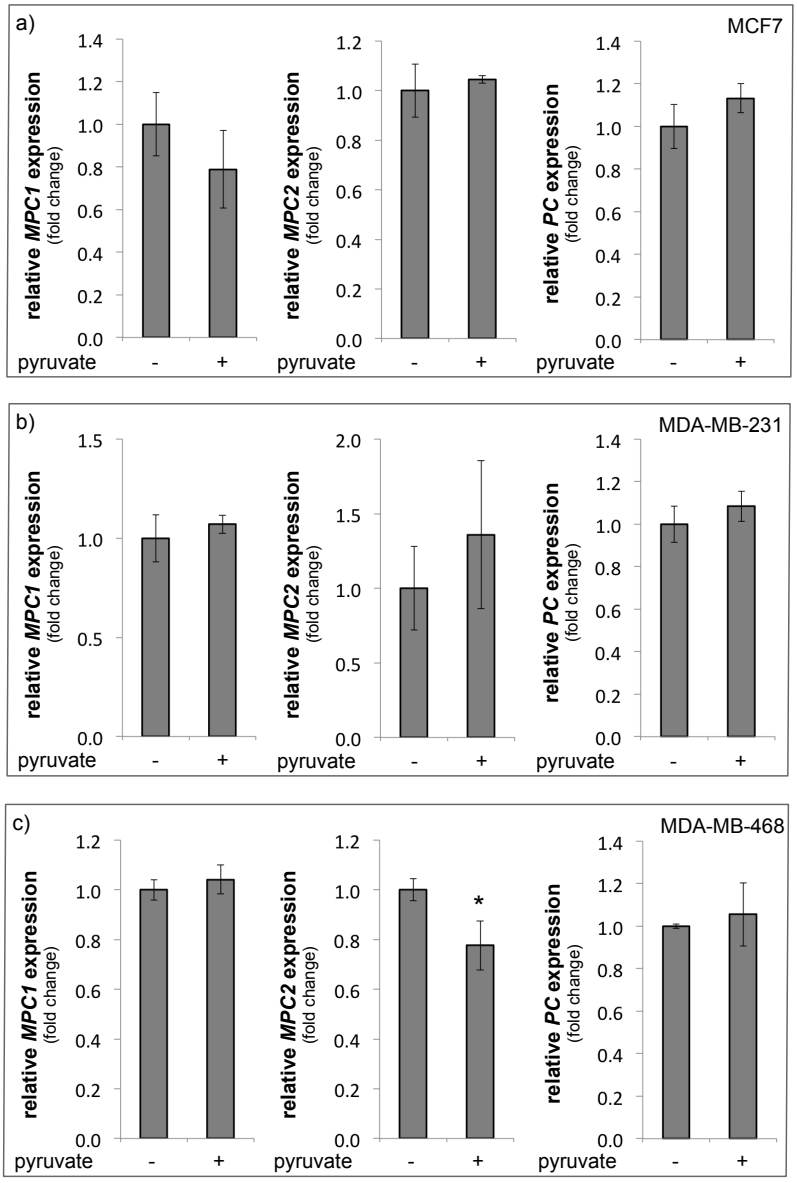

Figure S2: Pyruvate addition does not increase the gene expression of pyruvate transporting or converting proteins. *Related to Figure 3.*

Relative gene expression of the mitochondrial pyruvate transporter (*MPC1/2*) and pyruvate carboxylase (*PC*) in MCF7, MDA-MB-231, and MDA-MB-468 breast cancer cell lines after 24h without or with 5mM pyruvate addition to the nutrient microenvironment (n=3). Error bars depict standard deviation. * indicates $p \leq 0.05$ based on a two-tailed paired t-test.

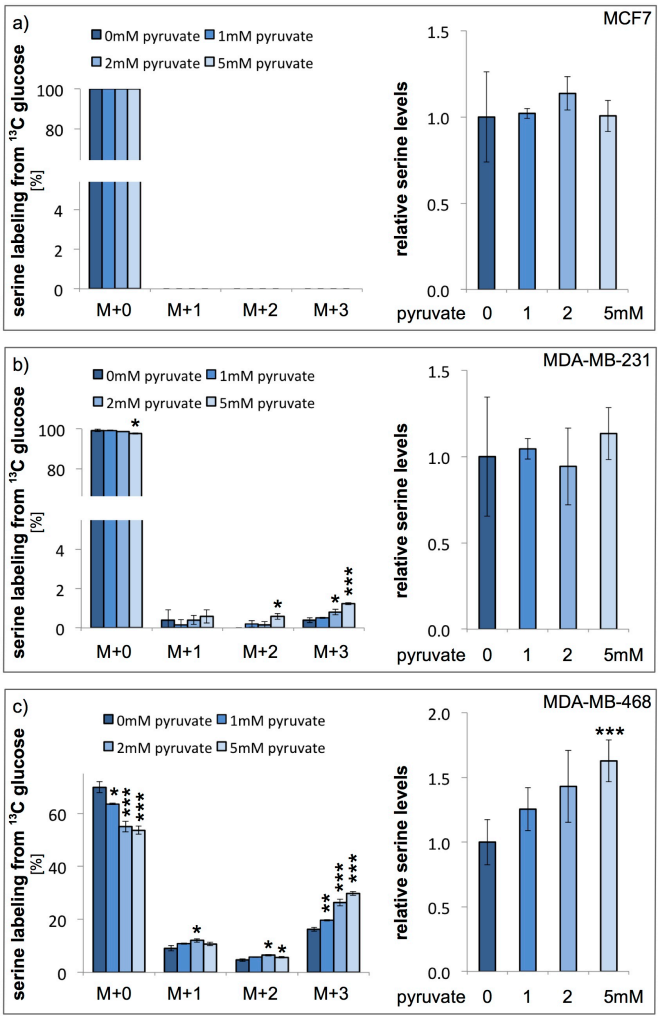

Figure S3: *De novo* serine biosynthesis is induced in MDA-MB-468 cells upon pyruvate addition to the nutrient microenvironment. *Related to Figure 4.*

a-c) *De novo* serine biosynthesis estimated using the ^{13}C enrichment of serine from $^{13}C_6$-glucose, and serine levels in different breast cancer cell lines upon pyruvate addition to the nutrient microenvironment (n≥3). Error bars depict standard deviation. * indicates $p \leq 0.05$, ** indicates $p \leq 0.01$, *** indicates $p \leq 0.005$ based on a two-tailed paired t-test.

Increased ATP coupled respiration without an increase in PDH flux (Figure 4c) or fatty acid oxidation (data not shown) is unusual. Yet, it can be explained by increased *de novo* serine biosynthesis. This pathway produces NADH, which can be transported via the malate-aspartate shuttle or via the glycerol-3-phosphate shuttle (in form of $FADH_2$) to the mitochondria and therefore contribute to ATP coupled respiration. Thus, we hypothesized that in MDA-MB-468 cells *de novo* serine biosynthesis is increased. We measured the ^{13}C enrichment of serine from $^{13}C_6$-glucose to assess *de novo* synthesized serine. In line with our hypothesis we found that MDA-MB-468 cells, differently from the other two cell lines, showed a substantial increase in the ^{13}C enrichment of serine from $^{13}C_6$-glucose and increased serine accumulation upon pyruvate addition to the nutrient microenvironment.

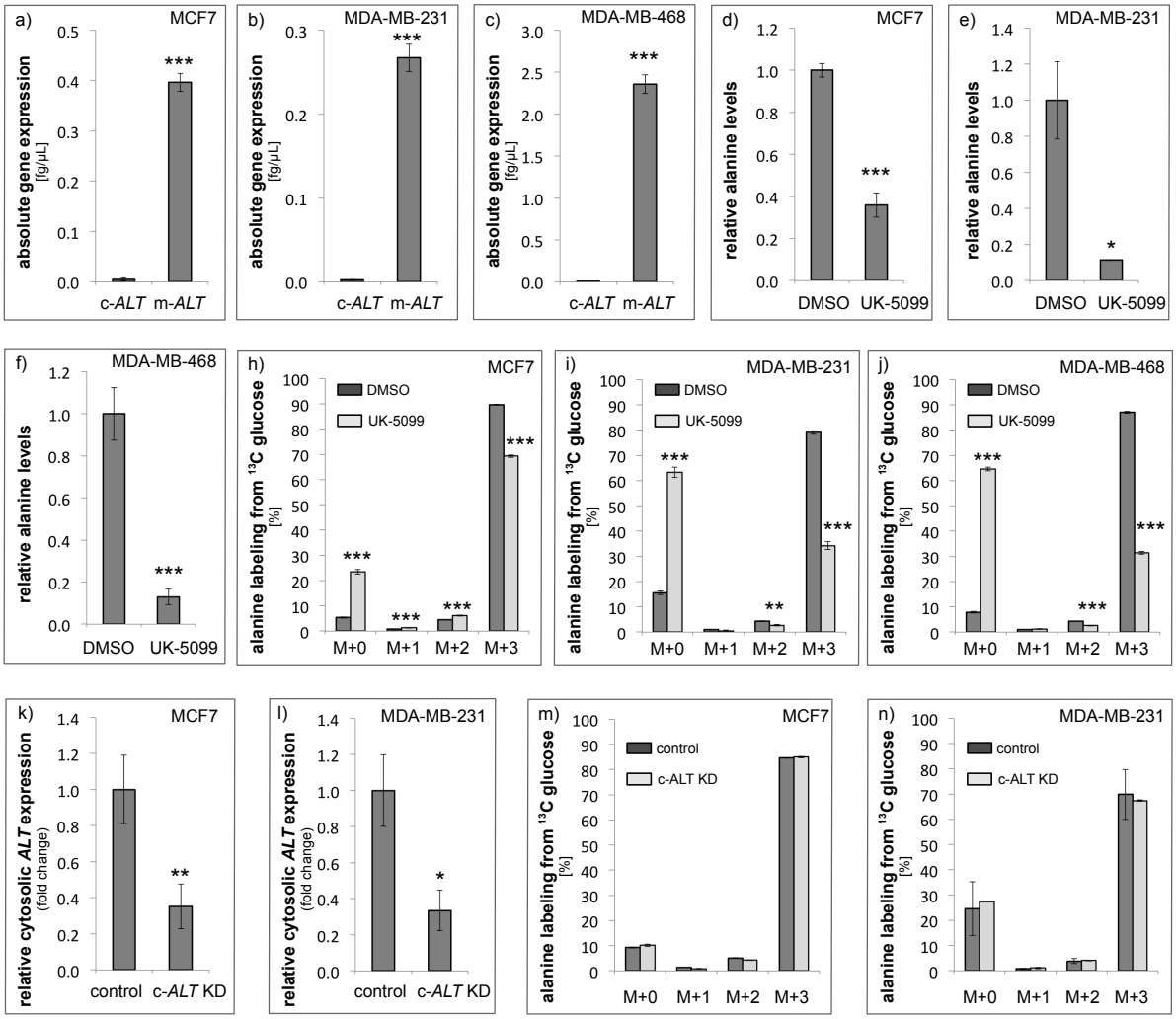

Figure S4: Cytosolic alanine aminotransferase activity is not detectable in breast cancer cell lines. *Related to Figure 5.*

a-c) Absolute concentration of cytosolic (c) and mitochondrial (m) alanine aminotransferase (*ALT*) mRNA in different breast cancer cell lines (n=3). d-e) Relative alanine levels upon treatment with the mitochondrial pyruvate transport inhibitor UK-5099 (10µM) in different breast cancer cell lines (n=3). h-j) ^{13}C enrichment of alanine from $^{13}C_6$-glucose upon treatment with the mitochondrial pyruvate transport inhibitor UK-5099 (10µM) in different breast cancer cell lines (n=3). k-l) Knockdown (KD) efficiency of cytosolic (c) aminotransferase (*ALT*) quantified by relative gene expression (n=3). m-n) ^{13}C enrichment of alanine from $^{13}C_6$-glucose upon knockdown (KD) of cytosolic (c) aminotransferase (ALT) (n=3). Error bars depict standard deviation. * indicates $p \leq 0.05$, ** indicates $p \leq 0.01$, *** indicates $p \leq 0.005$ based on a two-tailed paired t-test.

If alanine is produced predominately from mitochondrial pyruvate, then the expression of the cytosolic alanine aminotransferase should be very low compared to the expression of the mitochondrial alanine aminotransferase. Moreover, inhibition of pyruvate transport into the mitochondria using the pharmacologic inhibitor UK-5099 should reduce alanine levels and ^{13}C labeling from $^{13}C_6$-glucose if alanine is predominantly produced from mitochondrial pyruvate. Thus, we measured the expression of cytosolic and mitochondrial alanine aminotransferase, as well as alanine levels and ^{13}C labeling from $^{13}C_6$-glucose upon treatment with UK-5099. In line with the assumption that alanine is predominantly produced from mitochondrial pyruvate, we found that cytosolic alanine aminotransferase was expressed 85 to 546 times less than mitochondrial alanine aminotransferase in all tested breast cancer cell lines (Figure S4a-c). Moreover, alanine levels and alanine labeling from $^{13}C_6$-glucose were significantly reduced upon treatment with the MPC inhibitor UK-5099 (Figure S4d-j). Additionally, we tested cytosolic alanine aminotransferase knockdown cells and detected no significant change in the alanine labeling from $^{13}C_6$-glucose (Figure S4k-n). Thus, we concluded that mitochondrial pyruvate is the predominant substrate for *de novo* alanine biosynthesis in MCF7, MDA-MB-231, and MDA-MB-468 cell lines.

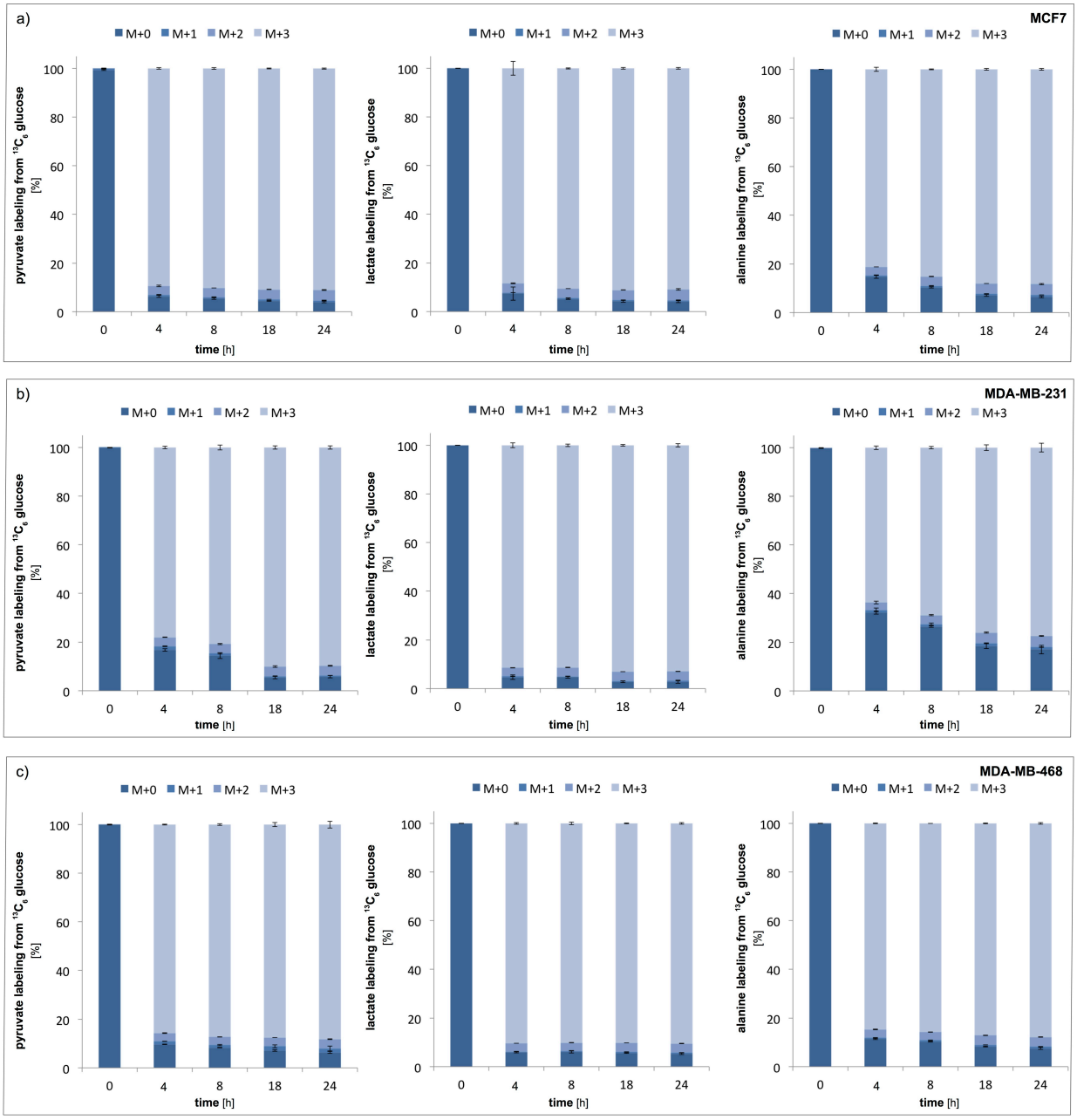

Figure S5: Labeling steady state is reached after 18h. *Related to Figure 5.*

a-c) Time resolved ^{13}C enrichment of pyruvate, lactate, and alanine from $^{13}C_6$-glucose in different breast cancer cell lines (n=3). Error bars depict standard deviation.

To exclude the possibility that alanine is not synthesized *de novo,* but derived from protein breakdown, we performed a ^{13}C labeling experiment with temporal resolution. We labeled MCF7, MDA-MB-231, and MDA-MB-468 cell lines for 4, 8, 18, and 24h with $^{13}C_6$ glucose and measured the ^{13}C enrichment in pyruvate, lactate, and alanine. If alanine, lactate, and pyruvate are produced *de novo* their ^{13}C enrichment should reach labeling steady state. However, if protein pools (which show a much slower turnover compared to free metabolites) are broken down, labeling steady state should not be reached within such a short time frame (Buescher et al., 2015). We found that alanine, lactate, and pyruvate reached labeling steady state within 18h in the tested cell lines. This verifies that protein breakdown is marginal or not present in the culture conditions we used.

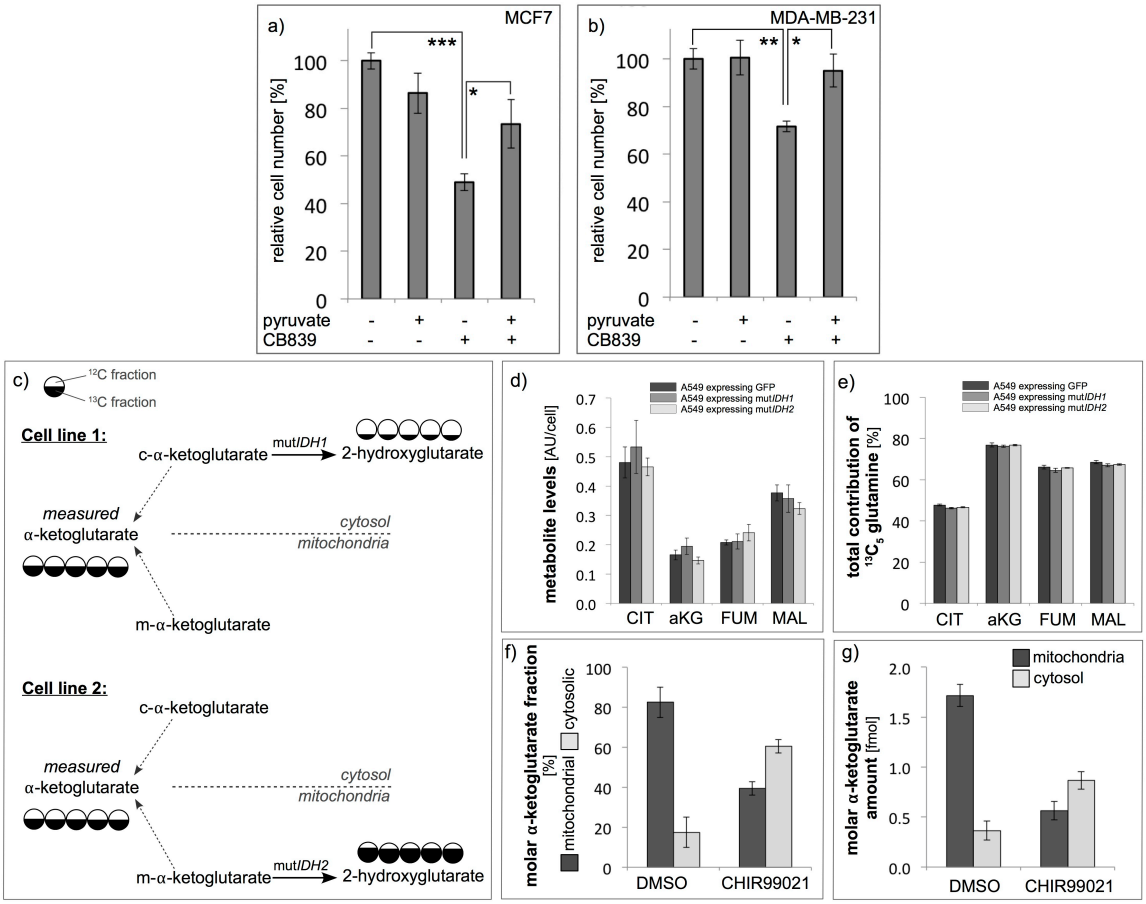

Figure S6: Pyruvate addition attenuates inhibition of glutamine anaplerosis and genetic engineering combined with our mathematical model allows estimating compartment-specific α-ketoglutarate levels. *Related to Figure 5 and 6.*

a-b) Relative cell number of breast cancer cells treated with the glutaminase inhibitor CB839 (200nM) in the presence and absence of 5mM pyruvate (n≥3). Error bars depict standard deviation. * indicates $p \leq 0.05$, ** indicates $p \leq 0.01$, *** indicates $p \leq 0.005$ based on a two-tailed paired t-test. c) Cells with mutant isocitrate dehydrogenase (mut*IDH*) 1 produce 2-hydroxyglutarate from cytosolic (c) α-ketoglutarate, while cells with mutant isocitrate dehydrogenase (mut*IDH*) 2 produce 2-hydroxyglutarate from mitochondrial (m) α-ketoglutarate. Thus, the molar fraction of mitochondrial and cytosolic α-ketoglutarate can be calculated based on the ^{13}C labeling patterns of 2-hydroxyglutarate and α-ketoglutarate. d-e) Metabolite levels and the total ^{13}C enrichment of metabolites from $^{13}C_5$-glutamine in A549 cells expressing GFP, mut*IDH*1 or mut*IDH*2. CIT refers to citrate, aKG refers to α-ketoglutarate, FUM refers to fumarate, MAL refers to malate. Mass distribution vectors are provided in Table S6. Error bars depict standard deviation. f-g) Molar fraction and molar amount of mitochondrial and cytosolic α-ketoglutarate in A549 cells treated with and without the GSK-3 inhibitor CHIR99021 (7μM), estimated based on our mathematical model (n=3). Mass distribution vectors are provided in Table S6. Error bars depict standard error.

We used two recently published cell lines that express very low amounts of mutant isocitrate dehydrogenase (IDH) 1 (cytosolic) or mutant IDH2 (mitochondrial)(Lewis et al., 2014) to provide a proof of concept for extending our mathematical model beyond pyruvate. The expression of low amounts of mutant IDH leads to the production of low amounts of 2-hydroxyglutarate from α-ketoglutarate. Depending on which mutant IDH isoform is expressed, the labeling patterns in 2-hydroxyglutarate represent the labeling patterns of either mitochondrial or cytosolic α-ketoglutarate (Figure S6c-e, Table S6). To verify the combination of the mathematical model with metabolic engineering, we tested whether we can recapitulate the recent finding that GSK-3 inhibition with CHIR99021 increases cytosolic α-ketoglutarate levels (Carey et al., 2015). Thus, we measured ^{13}C labeling in α-ketoglutarate and 2-hydroxyglutarate from $^{13}C_5$ glutamine in A549 cells with and without GSK-3 inhibitor, and analyzed the labeling data with our mathematical model, combing the resulting molar fractions with measured metabolite levels for α-ketoglutarate. Using our model, we could show that the cytosolic α-ketoglutarate fraction and molar amount increased upon GSK-3 inhibition (Figure S6f-g, Table S6).

Table S1-6

Table S1: MDVs from mouse tissue (see provided xls file). *Related to Figure 1.*

Table S2: MDVs from cell lines with and without pyruvate (see provided xls file). *Related to Figure 3.*

Table S3: Effects of pyruvate exchange flux between the mitochondria and the cytosol, cytosolic ME flux, and alanine cycling on MDVs needed for equation 15 (see provided xls file). *Related to Figure 5.*

Table S4: MDVs from published dataset (see provided xls file). *Related to Figure 5.*

Table S5: MDVs from MDA-MB-231 cells with and without UK-5099 (see provided xls file). *Related to Figure 6.*

Table S6: MDVs from engineered sensor system (see provided xls file). *Related to Figure S6.*

Supplemental Experimental Procedures

Mathematical model

This mathematical model can be used to determine the fractional distribution of pyruvate between the cytosol and the mitochondria. Combining this information with the cell average pyruvate concentrations and compartment volumes allow estimating the molar amount and the concentration of pyruvate in both compartments. Moreover, this model is based on the reporter metabolites alanine and lactate as surrogate for the mitochondrial and cytosolic labeling patterns of pyruvate, respectively. Consequently following requirements need to be met to use this model: i) the model is only valid *in vitro*, ii) pyruvate and alanine cannot be in the media formulation, iii) the biological system is in metabolic and labeling steady state, iv) LDH is cytosolic, v) cytosolic ALT flux producing alanine is marginal or not present compared to the mitochondrial ALT flux producing alanine, vi) protein breakdown is marginal or not present.
To estimate the fractional distribution of pyruvate between the cytosol and the mitochondria we labeled cells for 24h with $^{13}C_6$-glucose in DMEM containing 10% dialyzed serum and measured the metabolite labeling patterns by GC-MS as described below. We extracted the labeling patterns of pyruvate (MDV_P) lactate (MDV_L) and alanine (MDV_A) from the raw ion chromatograms using a custom Matlab M-file, which applies consistent integration bounds and baseline correction to each ion (Young et al., 2008). In addition, we corrected for naturally occurring isotopes using the method of Fernandez et al. (Fernandez et al., 1996). Negative values and mass overlaps were considered as zero and we corrected the mass spectra for potential metabolite contamination in a blank extraction.

$$x_M = \frac{MDV_P - MDV_L}{MDV_A - MDV_L} \quad \text{(eq 15)}$$

Equation 15 can be solved by either using M+0 or M+3 of lactate, alanine and pyruvate as input, or by using the entire MDVs as input. In the latter case we used the Matlab build-in function lscov to receive a solution for equation 15.

To determine the molar amount of pyruvate within the mitochondria ($n_{M\text{-}P}$) and the cytosol ($n_{C\text{-}P}$), we combined the results from equation 15 with the measured total molar amount of pyruvate (n_P) within an entire cell.

$$n_{M-P} = x_M * n_P \quad \text{(eq 16)}$$

$$n_{C-P} = (1 - x_M) * n_P \quad \text{(eq 17)}$$

Based on the molar amount of pyruvate within the mitochondria ($n_{M\text{-}P}$), the actual mitochondrial pyruvate concentration ($c_{M\text{-}P}$) was determined by estimating the cytosolic ($V_{C\text{-}P}$) and the mitochondrial ($V_{M\text{-}P}$) cell volume.

$$c_{M-P} = \frac{n_{M-P}}{V_{M-P}} \quad \text{(eq 18)}$$

To assess mitochondrial cell volume, we performed immunofluorescence staining of the plasma membrane and the mitochondria and total cell volume measurements with a MOXI Z Mini Automated Cell Counter (ORFLO) as described below.

^{13}C tracer analysis

All labeling experiments were performed in media with 10% dialyzed serum for 24h. All tracers were purchased from Sigma-Aldrich. In those cases were PC-dependent anaplerosis was determined in the presence of pyruvate, both glucose and pyruvate were ^{13}C labeled, to correct for label dilution from pyruvate uptake. Metabolites for the subsequent mass spectrometry analysis were prepared by quenching the cells in liquid nitrogen followed by a cold two-phase methanol-water-chloroform extraction (Fendt et al., 2013b). Phase separation was achieved by centrifugation at 4 °C. The methanol-water phase containing polar metabolites was separated and dried using a vacuum concentrator. Dried metabolite samples were stored at −80 °C. Polar metabolites were derivatized for 90 min at 37 °C with 7.5 µl of 20 mg ml^{-1} methoxyamine in pyridine and subsequently for 60 min at 60 °C with 15 µl of N-(tert-butyldimethylsilyl)-N-methyl-trifluoroacetamide, with 1% tert-butyldimethylchlorosilane (Fendt et al., 2013a) (Sigma-Aldrich). Mass distributions and metabolite concentrations were measured with a 7890A GC system (Agilent Technologies) combined with a 5975C Inert MS system (Agilent Technologies). 1 µl of sample was injected into a DB35MS column in splitless mode using an inlet temperature of 270 °C. The carrier gas was helium with a flow rate of 1 ml min^{-1}. Upon injection, the GC oven was held at 100 °C for 3 min and then ramped to 300 °C with a gradient of 2.5 °C min^{-1} followed by a 5 min after run at 320 °C. The MS system was operated under electron impact ionization at 70 eV and a mass range of 100–650 amu was scanned. Mass distributions were extracted from the raw ion chromatograms using a custom Matlab M-file, which applies consistent integration bounds and baseline correction to each ion (Young et al., 2008). In addition, we corrected for naturally occurring isotopes using the method of Fernandez *et al.* (Fernandez et al., 1996). Negative values and mass overlaps were considered as zero. We corrected the mass spectra for potential metabolite contamination in a blank extraction. All labeling fractions were transformed to a natural abundance corrected mass distribution vector (MDV) (Buescher et al., 2015). Relative changes in PC-dependent anaplerosis were estimated based on the difference between malate M+3 and succinate M+3 from $^{13}C_6$-glucose, under the prerequisite that pyruvate enrichment is similar in the compared conditions. Metabolite levels were determined based on metabolite standards, the internal standards norvaline and glutarate, and cell numbers counted with a hemocytometer. In case of tissue samples, tissue weight was used for normalization of metabolomics data.

Flux model for the simulation of MDVs

'Glc.x (abcdef) => PEP (cba) + PEP (def) '
'PEP (abc) => Pyr.c (abc) '
'Pyr.c (abc) => Lac (abc)'
'Lac (abc) => Lac.x (abc)'
'Pyr.m (abc) + CO2 (d) => Oac (abcd)'
'Mal (abcd) => Pyr.m (abc) + CO2 (d)'
'Pyr.m (abc) => AcCoA (bc) + CO2 (a)'
'AcCoA (ab) + Oac (cdef) => Cit (fedbac)'
'Cit (abcdef) => Akg (abcde) + CO2 (f)'
'Akg (abcde) => Suc (bcde) + CO2 (a)'
'Suc (abcd) <=> Fum (abcd)'
'Fum (abcd) <=> Mal (abcd)'
'Mal (abcd) <=> Oac (abcd)'
'Pyr.m (abc) => Ala (abc)'
'Oac (abcd) => Asp (abcd)'
'Gln.x (abcde) => Gln (abcde)'

'Gln (abcde) <=> Glu (abcde)'
'Glu (abcde) <=> Akg (abcde)'
'Asp (abcd) => Biomass'
'Cit (abcdef) => Biomass'
'Ala (abc) => Biomasse'
'Pyr.c (abc) <=> Pyr.m (abc)'
'0 Pyr.c (abc) => Pyr.mnt (abc)'
'0 Pyr.m (abc) => Pyr.mnt (abc)'
'Pyr.mnt (abc) => Pyr.fix (abc)'
'Ala (abc) => Pyr.c (abc)'
'Mal (abcd) => Pyr.c (abc) + CO2 (d)'

Assumptions:
- the system is in steady state
- all CO_2 in the system is unlabeled
- fumarate and succinate have no orientation, because they are symmetrical
- alanine, aspartate and citrate (via fatty acids and aspartate production) contribute to biomass
- pyruvate MDVs reflect cell average labeling patterns

Interstitial fluid and blood plasma collection

The collection of interstitial fluid from mouse lungs was performed as described before (Wiig et al., 2003). The tissue was cut and placed into test tubes with perforated bottom. 20 µL of 0.9% NaCl solution pH 7.4 was added to the tissue sample. Interstitial fluid was collected by centrifugation (110 g, 10 min, 4°C). Blood plasma was harvested by centrifugation (12000g, 10min). Protein within the interstitial fluid or blood plasma was precipitated using −20°C cold methanol/water-mix (5:3) subsequent centrifugation (21130g, 2 min, 4°C). The supernatant was dried using a vacuum centrifuge and derivatized for mass spectrometry analysis.

PDH flux

The decarboxylation of pyruvate was assessed using 1-^{14}C-pyruvate. Cells were preincubated in DMEM containing 1mM or 5mM unlabeled pyruvate. The assay medium, containing labeled 1-^{14}C-pyruvate (500 µCi/mmol) and 1mM or 5mM cold pyruvate, was incubated at 37°C for 2h to allow evaporation of $^{14}CO_2$ produced from spontaneous decarboxylation, after which specific activity was determined. For assessment of PDH-flux, cells were incubated with assay medium for 15min (MCF7 and MDA-MB-468) or 25min (MDA-MB-231) at 37°C. To stop cellular metabolism, perchloric acid (0.2 ml 12% $HClO_4$) was added and wells were immediately covered with Whatman filter papers (2.6 cm x 2.6 cm) soaked in hyamine. Subsequently, the 12-well plate was rapidly sealed to allow absorption of $^{14}CO_2$ produced during pyruvate decarboxylation. One hour later, the filter papers were transferred to scintillation vials and radioactivity was measured using by liquid scintillation counting. Wells containing culture medium but no cells were used to establish background levels of $^{14}CO_2$. Data were corrected for label dilution due to pyruvate uptake (Buescher et al., 2015).

Oxygen consumption rates

Oxygen consumption was measured with an Oxytherm Clark electrode instrument (Hansatech). After a 24h treatment with or without pyruvate (5mM) and oligomycin A (1µM), cells were trypsinized and resuspended in fresh media with at least 2 x 10^6 cells ml^{-1} for measurements. The oxygen consumption rate of cells in suspension was measured for 10 min at 37°C. The slope of the linear range was used to calculate rates based on cell number counts. The ATP-coupled mitochondrial oxygen consumption rate was calculated as difference between total oxygen consumption rates and oxygen consumption rates after oligomycin A treatment.

Immunofluorescence microscopy

An immunofluorescence staining of plasma membrane and mitochondria was performed. Cells cultured with or without pyruvate (5mM) were fixed with formaldehyde (4.5%) before staining with Alexa Fluor 555-conjugated wheat germ agglutinin WGA (Thermo Fisher Scientific). After several HBSS washes, cells were subsequently permeabilized with 0.5% Triton-X-100 2% BSA for 30 min, blocked with 2% BSA and 5% donkey serum for 1h, and incubated overnight with TOMM20 antibody (1:200) (Abcam ab56783) at 4°C in a moist chamber. After several PBS washes, cells were incubated for 2h with Alexa Fluor 488-conjugated anti-Ig secondary antibody (1:1000) (Thermo Fisher Scientific). After several PBS washes, nucleus staining was carried out with Topro-3 according to the manufacturer instructions (Thermo Fisher Scientific). All microscopy and imaging analyses were performed in the Bio Imaging core facility of VIB. Images were acquired using a confocal Leica SP5 microscope based on Z-stacks of 0.2µm and a zoom factor of 3. Finally, 3D total and mitochondrial volumes were reconstructed using Imaris 8.2.1 software (Bitplane) and averaged over 10 cells. The mitochondrial volume fraction was calculated based on the 3D reconstructions. Total cell volume (in µl) was measured using a MOXI Z Mini Automated Cell Counter (ORFLO), which is based on the principle that cells passing through an electric current cause a momentary increase in voltage directly proportional to the cell volume. Total cell volume was multiplied times the mitochondrial volume fraction to obtain the total mitochondrial cell volume.

Acetyl-CoA and ATP/ADP measurements

The dried metabolite samples for acetyl-CoA measurements were resuspended in 1 % percholoric acid and transferred to LC-MS vials. Measurements were performed using a Dionex UltiMate 3000 LC System (Thermo Scientific) coupled to a Q Exactive™ Orbitrap mass spectrometer (Thermo Scientific) operated in positive mode. 90 µl of sample was separated on a Acquity UPLC HSS T3 column (Waters). We further applied a solvent gradient described before (Basu et al., 2011). Data collection was performed using Xcalibur™ software (Thermo Scientific).
Polar metabolites for ATP/ADP measurements were resuspended in 60% acetonitrile. Metabolites were measured using a Dionex UltiMate 3000 LC System (Thermo-Scientific) combined with a Q Exactive™ Orbitrap mass spectrometer (Thermo Scientific) operated in negative mode, using untargeted mass spectrometry. Samples were injected onto a iHilic-Fusion(P) (Hilicon). The solvent, composed of acetonitrile and ammonium acetate (pH=9.3, 10mM), was fed at a flow rate of 0.100ml/min. Data analysis was performed with Xcalibur™ software (Thermo Scientific).

Genetic manipulations and qPCR

The shRNA plasmid against cytosolic ALT (ID NM_005309.1-1128s1c1: Sigma-Aldrich) contained the following clone, target sequence: CCGG CTCA TTCA AGAA GGTG CTCA TCTC GAGA TGAG CACC TTCT TGAA TGAG TTTT TG. The target sequence was cloned into the lentiviral plasmid pLKO.1-TRC puromycin. Knockdowns were verified based on gene expression (Figure S4).

Total RNA was isolated from 2-10mg of snap-frozen mouse liver tissue using lysing matrix D spherical tubes (MP Biomedicals) and TRIzol Reagent (Thermo Fisher Scientific). Total RNA from cultured cell lines was isolated using the Purelink RNA Mini kit (Thermo Fisher Scientific). Single strand cDNA was synthetized from 1µg of total RNA using the qScript cDNA synthesis kit (Quantabio). Real-time quantitative PCR (RT-qPCR) was performed on a Viia7 instrument (Applied Biosystems) using a platinum SYBR green qPCR supermix UDG (Thermo Fisher Scientific). In order to obtain the absolute quantification of cytosolic alanine aminotransferase, we ran a standard curve of known concentrations of cDNA together with the sample cDNA on the RT-qPCR instrument. The standard cDNA was obtained using the PCR mastermix 2X (Thermo Fisher Scientific) according to the manufacturer's protocol. The cDNA was loaded on a 1.5% agarose gel and run for 30 minutes at 135V. Afterwards, the cDNA was purified using the geneclean spin kit (Qbiogene) according to the manufacturer's protocol, and dilutions were made (1pg up to 1-10pg). Primers used for analysis are listed below:

species	gene name	primer direction	*sequence*
mouse	*cyclophilin*	*FW*	*5'-CTTCTTGCTGGTCTTGCCATTCCT-3'*
		REV	*5'-GGATGGCAAGCATGTGGTCTTTG-3'*
mouse	*MPC1*	*FW*	*5'-ATGTCCGGAGCAAGGACTTC-3'*

		REV	*5′-ACAGAGGGCGAAAGTCATCC-3′*
mouse	*MPC2*	*FW*	*5′-CCAAAGAAATTGAGGCCGCT-3′*
		REV	*5′-GACCAAATAAACCCTGTAGCCATC-3′*
mouse	*MCT1*	*FW*	*5′-TTGCCCCTTTGTCTACAACC-3′*
		REV	*5′-CCTCCGCTTTCTGTTCTTTG-3′*
mouse	*MCT4*	*FW*	*5′-GACAGAGGCAGATACAGCGG-3′*
		REV	*5′-GAGGGCTGCTTTCACCAAGA-3′*
mouse	*PC*	*FW*	*5′-GCCCAGAAGTTGCTACATTACCT-3′*
		REV	*5′-CTCACATTGACAGGGATTGGA-3′*
human	*RPL19*	*FW*	*5′-AGTATGCTCAGGCTTCAGAAGA-3′*
		REV	*5′-ATTGGTCTCATTGGGGTCTAAC-3′*
human	*MPC1*	*FW*	*5′-GCCACGCAACAAATGAAGTA-3′*
		REV	*5′-TGCAGATGCCGTTTTAGTCA-3′*
human	*MPC2*	*FW*	*5′-AGCAGGAGCCTCTCAGCTTT-3′*
		REV	*5′-GTCCCAATGGTTTTGTCCAC-3′*
human	*MCT1*	*FW*	*5′-CCAGCGAAGTGTCATGGATA-3′*
		REV	*5′-AAGCAGCCACCAACAATCAT-3′*
human	*MCT4*	*FW*	*5′-CGGCTTTGTGCTTTACGCC-3′*
		REV	*5′-GCTGAAGAGGTAGACGGAGTA-3′*
human	*PC*	*FW*	*5′-CCAGAGGCAGGTCTTCTTTG-3′*
		REV	*5′-GGGTGAGGTCACCACAGTCT-3′*
human	*ALT1* (cytosolic)	*FW*	*5’-GTGCGCTCTGTGTCATCAAC-3’*
		REV	*5’-GTCCGCCAGCAGAAAGAG-3’*
human	*ALT2* (mitochondrial)	*FW*	*5′-ACCCCGACAACATCTACCTG-3′*
		REV	*5′-ATCATCACACCTGTCCGTGA-3′*

Mouse models and in vivo ^{13}C tracer analysis

Female BALB/c mice were orthotopically inoculated with one million 4T1 cells. Primary cancer growth and bodyweight was monitored every second day. Two weeks after cancer initiation, surgical catheterization of the jugular vein was performed as follows: BALB/c mice were anesthetized with 1% isoflurane and a catheter was placed into the right jugular vein. A small incision between shoulder blades was made and the catheter was exteriorized at the back of the mouse and connected to an antenna part, which enables conscious handling of the mouse during infusion. The tubing was flushed with heparinized saline directly after the surgery and 3 days later. Animals were individually housed after surgery, and painkillers were administered (Carprofen, 5mg kg^{-1} body weight subcutaneous) during surgery and one day after (Davidson et al., 2016; Quaegebeur et al., 2016). 7 days after surgery, $^{13}C_6$-labeled glucose (99% enriched; Sigma-Aldrich) infusions were conducted. Mice were subjected to a continuous infusion of 0.03 mg ^{13}C labeled glucose per gram body weight per minute over the course of 6 hours. Subsequently, mice were sacrificed using nembutal, blood was collected and the breast cancers and lung metastases were placed in cold saline, dissected in less than 3 min, and immediately frozen using a liquid nitrogen cooled Biosqueezer (Biospec Products). The tissue was weighed (10-15mg) and pulverized (Cryomill, Retsch) under liquid nitrogen conditions. The pulverized tissue was extracted for GC-MS analysis as described above.

References

Basu, S.S., Mesaros, C., Gelhaus, S.L., and Blair, I.A. (2011). Stable Isotope Labeling by Essential Nutrients in Cell Culture for Preparation of Labeled Coenzyme A and Its Thioesters. Analytical Chemistry *83*, 1363-1369.

Buescher, J.M., Antoniewicz, M.R., Boros, L.G., Burgess, S.C., Brunengraber, H., Clish, C.B., DeBerardinis, R.J., Feron, O., Frezza, C., Ghesquiere, B., et al. (2015). A roadmap for interpreting ^{13}C metabolite labeling patterns from cells. Current Opinion in Biotechnology *34*, 189-201.

Carey, B.W., Finley, L.W.S., Cross, J.R., Allis, C.D., and Thompson, C.B. (2015). Intracellular α-ketoglutarate maintains the pluripotency of embryonic stem cells. Nature *518*, 413-416.

Davidson, Shawn M., Papagiannakopoulos, T., Olenchock, Benjamin A., Heyman, Julia E., Keibler, Mark A., Luengo, A., Bauer, Matthew R., Jha, Abhishek K., O'Brien, James P., Pierce, Kerry A., et al. (2016). Environment Impacts the Metabolic Dependencies of Ras-Driven Non-Small Cell Lung Cancer. Cell metabolism *23*, 517-528.

Fendt, S.M., Bell, E.L., Keibler, M.A., Davidson, S.M., Wirth, G.J., Fiske, B., Mayers, J.R., Schwab, M., Bellinger, G., Csibi, A., et al. (2013a). Metformin Decreases Glucose Oxidation and Increases the Dependency of Prostate Cancer Cells on Reductive Glutamine Metabolism. Cancer research *73*, 4429-4438.

Fendt, S.M., Bell, E.L., Keibler, M.A., Olenchock, B.A., Mayers, J.R., Wasylenko, T.M., Vokes, N.I., Guarente, L., Vander Heiden, M.G., and Stephanopoulos, G. (2013b). Reductive glutamine metabolism is a function of the α-ketoglutarate to citrate ratio in cells. Nature communications *4*, 2236.

Fernandez, C.A., Des Rosiers, C., Previs, S.F., David, F., and Brunengraber, H. (1996). Correction of 13C Mass Isotopomer Distributions for Natural Stable Isotope Abundance. Journal of Mass Spectrometry *31*, 255-262.

Lewis, C.A., Parker, S.J., Fiske, B.P., McCloskey, D., Gui, D.Y., Green, C.R., Vokes, N.I., Feist, A.M., Vander Heiden, M.G., and Metallo, C.M. (2014). Tracing Compartmentalized NADPH Metabolism in the Cytosol and Mitochondria of Mammalian Cells. Mol Cell.

Quaegebeur, A., Segura, I., Schmieder, R., Verdegem, D., Decimo, I., Bifari, F., Dresselaers, T., Eelen, G., Ghosh, D., Davidson, S.M., et al. (2016). Deletion or Inhibition of the Oxygen Sensor PHD1 Protects against Ischemic Stroke via Reprogramming of Neuronal Metabolism. Cell metabolism.

Wiig, H., Aukland, K., and Tenstad, O. (2003). Isolation of interstitial fluid from rat mammary tumors by a centrifugation method. American Journal of Physiology - Heart and Circulatory Physiology *284*, H416-H424.

Young, J.D., Walther, J.L., Antoniewicz, M.R., Yoo, H., and Stephanopoulos, G. (2008). An elementary metabolite unit (EMU) based method of isotopically nonstationary flux analysis. Biotechnology and bioengineering *99*, 686-699.